Geodetic constraints on contemporary deformation in the northern Walker Lane: 3, Central Nevada Seismic Belt postseismic relaxation

William C. Hammond, Corné Kreemer
and Geoffrey Blewitt

Nevada Bureau of Mines and Geology and
Nevada Seismological Laboratory
University of Nevada, Reno, NV 89557-0178

April 2007

ABSTRACT

We combine horizontal GPS velocities, results from an Interferometric Synthetic Aperture Radar (InSAR) study, and paleoseismic data from the U.S.G.S. Quaternary Fault and Fold Database to evaluate the postseismic response of historic earthquakes in the Central Nevada Seismic Belt. The GPS data are from a new compilation of published and new GPS velocities that measure tectonic deformation of the Basin and Range province. We assume that the GPS velocity at each site has contributions from time-invariant (i.e. steady permanent crustal deformation accommodated with slip on faults that occurs over many seismic cycles) and transient (i.e. time varying and associated with the seismic cycle) processes that are attributable to postseismic viscoelastic relaxation of the crust and upper mantle. In order to infer the viscosity structure of the Basin and Range lower crust η_{LC} and upper mantle η_{UM} we apply three objective criteria to identify rheological models that fit both geodetic and geologic data. The model must (1) improve the apparent mismatch between geodetically and geologically inferred slip rates, (2) explain the InSAR results in terms of vertical uplift, and (3) not imply time-invariant contractions anywhere in the extending province. It is not required that the postseismic deformation field resemble the time-invariant velocity field in pattern, rate or style. We evaluate the relative strength of the different types of data we use, and find that the InSAR and horizontal GPS velocities form complementary constraints on the viscoelastic structure, excluding different parts of the model space. The best fitting model has a lower crust that is stronger than the uppermost mantle, with $\eta_{LC}=10^{20.5}$ Pa·s and $\eta_{UM}=10^{19}$ Pa·s, a finding that is consistent with the majority of similar studies in the Basin and Range. The best fitting viscosity model implies that the majority of the deformation

observed at the CNSB is attributable to postseismic relaxation, and hence that western Basin and Range time-invariant deformation north of 39°N latitude is more tightly focused into the Northern Walker Lane than would be inferred from the uncorrected GPS velocities. However, significant deformation remains after correction for postseismic effects, consistent with the depiction of the CNSB as a zone of active faulting intermediate in rate between the Walker Lane Belt and the central Basin and Range.

INTRODUCTION

Rates of slip on active continental faults inferred from geodetic techniques sometimes disagree with the rates inferred from geologic studies. This discrepancy lies near the heart of the relationship between geodetic and geologic investigations of continental deformation (e.g. Friedrich et al., 2003). Similarity of space geodetic and geologic measurement of lithospheric plate motions (DeMets and Dixon, 1999; Sella et al., 2002) has led to anticipation that agreement might occur on the smaller scale of individual faults as well. Where these rates agree, geodetic measurement of relative motions across the fault match the rate inferred from coseismic rupture offset and time between major slip events. However, the comparison requires making a correction of the geodetic data according to the buried dislocation model, comprised of a faulted half space locked at the surface but slipping at depth (Savage and Burford, 1973; Freund and Barnett, 1976). In this case the cumulative offset of many episodic surface ruptures from the largest earthquakes adds up to the slip predicted by far field motion of crustal blocks. Some faults, such as the relatively linear and simple San Andreas in Central California,

67 exhibit a close agreement (e.g. Murray et al., 2001). This suggests that paleoseismic
68 studies and geodesy measure the same physical processes at play in active faulting, albeit
69 over greatly different time scales, and different parts of the seismic cycle. Hence,
70 disagreement between paleoseismic and geodetic slip rates suggests that an explanation is
71 required for the deviation from this paradigm, and perhaps a modification of our physical
72 model.

73 The Central Nevada Seismic Belt (CNSB), which resides near the middle of the
74 Basin and Range Province (Wallace, 1984b), is a well documented example of
75 disagreement between slip rates estimated with geodetic and geologic techniques. The
76 CNSB is a quasi-linear sequence of large magnitude historical earthquakes that form an
77 approximately north-south trending belt (Figure 1) (Caskey et al., 2000). The CNSB
78 remains seismically active to this day, and is responsible for a large proportion of the
79 total historic seismic moment released in the Basin and Range (Pancha et al., 2006).
80 Paleoseismically inferred slip rates for the set of faults that comprise the belt near latitude
81 39˚N total probably less than 1 mm/yr (Bell et al., 2004). Geodetic rates, however,
82 inferred mostly from surveys with the Global Positioning System (GPS) are closer to 3-4
83 mm/yr (Thatcher et al., 1999; Bennett et al., 2003; Hammond and Thatcher, 2004), a
84 difference that is well outside the uncertainties in the measurements.

85 Recognition of the CNSB as a zone of recent earthquakes is essential to
86 explaining the discrepancy between geodetic and geologic rates because it allows for the
87 possibility of geodetic strain rates being influenced by transient post-seismic relaxation.
88 A number of studies have identified a postseismic response to large earthquakes that has
89 been explained by the viscoelastic properties of the Earth's lower crust and upper mantle

90 (starting with Nur and Mavko, 1974 and Savage and Prescott, 1978). The transient
91 postseismic part of the earthquake cycle may not be detectable in some cases because the
92 response decreases to zero over time, and the time since the last earthquake may have
93 been long. Recent progress in modeling the time dependent surface deformation
94 response (Pollitz, 1997) has made practicable the quantitative constraint of the viscous
95 component of the rheology based on geodetic data.

96 In what follows we present a new approach for constraining the viscoelastic
97 properties of the lower crust and upper mantle. We apply three types of complementary
98 data: horizontal GPS velocities, Interferometric Synthetic Aperture Radar (InSAR) that is
99 predominantly sensitive to vertical motion, and paleoseismic estimates of fault slip rates
100 and style. When comparing deformation measured with geodesy (e.g. GPS and InSAR)
101 to deformation inferred from geology we must account for the very different time scales
102 measured with these techniques. In this study we define time-invariant motion as the
103 hypothetical steady tectonic deformation that occurs at a constant rate over many seismic
104 cycles (e.g. associated with steady motion of the Sierra Nevada with respect to the Great
105 Basin). We refer to transient motions as those that vary over time-scales on the order of
106 the seismic cycle (e.g. exponentially decaying postseismic relaxation of viscous material
107 in the Earth). Because motions that are measured with GPS at any given time are
108 influenced by time-invariant and transient contributions, we cannot separate these
109 processes if we assume that the predicted relaxation signal resembles the GPS velocity
110 field. Instead we here assume that the paleoseismic data constrain the time-invariant
111 component of deformation, while physical models of viscoelastic relaxation constrain the
112 complementary transient motion.

In our modeling we calculate the postseismic velocities expected from the historic earthquakes in the CNSB and many assumed viscoelastic Earth models, where we vary the viscosity of the lower crust and upper mantle. From each model we infer the associated time-invariant deformation patterns by subtracting the transient component from the GPS velocities. To evaluate each model we use misfit criteria based on three types of data: GPS velocities, Interferometric Synthetic Aperture Radar results (InSAR), and geologic estimates of fault slip rates. The best models must 1) explain the discrepancy between geologic and geodetic slip rate at the CNSB, 2) explain the vertical motion observed with InSAR, and 3) not predict time-invariant contractions anywhere in the extensional Basin and Range province. From the best fitting viscoelastic Earth model we obtain the most likely postseismic relaxation two-dimensional surface velocity pattern present inside the current snapshot of the geodetic velocity field. We then present the deformation patterns implied by the estimated time-invariant velocity field, and how they differ from the apparent motion gleaned directly from GPS and other geodetic studies.

DATA

Historic Earthquakes of the Central Nevada Seismic Belt

We consider seismic events in central Nevada occurring in the last 150 years that had magnitude of approximately 6.5 or above (Table 1). The amount of postseismic motion that a GPS site might detect is a function of the size of the earthquake, its style and orientation, and the time and distance between the event and observation (Pollitz,

136 1997). For the earthquakes used here (simplified surface traces shown in Figure 1), these
137 parameters are constrained by geologic and paleoseismic investigation of the earthquake
138 surface ruptures, seismic data, and eyewitness accounts of the earthquakes. Details of the
139 earthquakes are discussed below, and the parameters used in the modeling are in listed
140 Table 1. Our estimates of the moment magnitude M_W are, in all cases, within 0.2 of the
141 estimates made by Pancha et al., (2006) for the largest earthquakes in the Basin and
142 Range Province.
143
144 **Earthquake Characteristics**
145
146 ***Owens Valley (1872) M_W 7.6.***
147 This event was likely the largest to occur in the Basin and Range Province in historic
148 time (Pancha et al., 2006), and is the earliest and southernmost event considered. Its
149 mechanism was predominantly right lateral strike slip with a minor amount of normal,
150 down to the east slip (Beanland and Clark, 1994). The estimated times of previous events
151 on this fault imply that its Holocene slip rate (2-4 mm/yr) (Lee et al., 2001) is among the
152 fastest in the Province. Geodetic rates (5-7 mm/yr) are even faster, however, and post-
153 seismic relaxation following the 1872 event has been invoked as a possible explanation
154 for this apparent discrepancy (Miller et al., 2001a; Dixon et al., 2003).
155
156 ***Pleasant Valley (1915) M_W 7.4.***
157 Occurring at the northern end of the CNSB, this event was recorded with early-generation
158 seismic instrumentation that was sufficient to characterize its size and tensor moment

159 (Doser, 1988) and produced 59 km of surface rupture (Wallace, 1984a) that is clearly
160 visible today. Its mechanism was predominantly normal, with extension oriented
161 N65˚W.
162
163 ***Cedar Mountain (1932) M_W 7.1***.
164 The rupture from this earthquake crossed through three valley fault systems, activating
165 north-south striking right-lateral strike slip faults in Monte Cristo Valley, right lateral and
166 normal faults in Stewart Valley, and secondary north-northeast striking normal faulting in
167 Gabbs Valley (Bell et al., 1999). The seismic data favor a predominantly strike-slip
168 earthquake on a fault dipping steeply to the east, containing two sub-events separated by
169 10 seconds (Doser, 1988). In our modeling the combined static stress changes of both
170 events are what initiate and drive the postseismic response, so we simplify the
171 calculations by assuming a single event that has the surface trace and combined moment
172 of both sub-events.
173
174 ***Rainbow Mountain, Fourmile Flat, Stillwater (1954) M_W 7.0***.
175 These events occurred in July and August in the same year and prior to the Fairview
176 Peak, Dixie Valley earthquake sequence (Caskey et al., 2004). Their surface traces lie
177 mostly in the eastern part of the Carson Sink, one valley west of the Fairview Peak, Dixie
178 Valley sequence (Caskey et al., 2004). The Stillwater (M_S 7.0) event was the largest
179 (Doser, 1986) but was similar to the others in style, being comprised of a combination of
180 right lateral and down to the west normal slip. Because of their similar style and close

proximity in time, in our modeling we combine these events into a single event with the combined moment of all three.

Fairview Peak (1954) M_W 7.0.

The coseismic offset parameters for this event are constrained by a combination of paleoseismic (Slemmons, 1957; Caskey et al., 1996) and geodetic data (Savage and Hastie, 1969; Snay et al., 1985; Hodgkinson et al., 1996). Slip was right lateral and normal on an east-dipping fault. This rupture, and the ones discussed below, occupy the middle latitudes of the CNSB and are hence transitional between the predominantly strike slip faults to the south (e.g., Owens Valley and Cedar Mountain) and normal ruptures to the north (e.g., Pleasant Valley). The prior event on this fault was likely over 35,000 ago (Caskey et al., 2000).

Dixie Valley (1954) M_W 6.9.

This event followed the Fairview Peak event by 4 minutes, and ruptured the western range front fault in the valley immediately to the north (Slemmons, 1957). Paleoseismic, geodetic and seismic data all indicate that it occurred on an east-dipping rupture plane accommodating mostly normal offset (Doser, 1986; Caskey et al., 1996; Hodgkinson et al., 1996). Thus this event is similar to the Pleasant Valley earthquake, which is the next and northernmost event to the north.

Gold King, Louderback, West Gate (1954) M_W 6.5.

These faults likely ruptured simultaneously with the Fairview Peak event. They are west-dipping, and lie just north of the Fairview peak rupture. Their distribution is more complex than the other faults, but are thought to have acted as a geometric link between the ruptures of the Dixie Valley and Fairview Peak earthquakes (Caskey et al., 2000). Individually and combined they are smaller than the Fairview Peak and Dixie Valley events, so we represent these three ruptures in our modeling as a single event and fault plane consisting of normal and strike-slip offset. Collectively these three events comprise the smallest event that we consider.

Examination of our final model shows that the smallest earthquakes we consider, the Gold King/Louderback/West Gate sequence (Table 1: M_W 6.5) contributes at most 0.15 mm/yr to the observed GPS velocity field (compared to 2.1 mm/yr for the Owens Valley event). Although some large earthquakes may have occurred in the past (prehistory) that could contribute to transient signals in our GPS data, we have used all the known earthquakes that can significantly affect our results. Given viscosities in the range of 10^{17}-10^{21} Pa·s (see Table 2 and references therein), a shear modulus of $3x10^{10}$ Pa, viscous Maxwell relaxation times are on the order of 0.1-1,000 years. Yet CNSB recurrence intervals are on the order of 5,000-35,000 years (Caskey et al., 2000; Bell et al., 2004; Wesnousky et al., 2005). Thus the GPS measurements were made very early in the seismic cycle for CNSB faults. Because the expected relaxation times are so much shorter than the recurrence intervals, the effects from the penultimate earthquakes are almost certainly negligible and are not modeled.

Global Positioning System Data

We use the horizontal GPS velocities from the compilation of Kreemer et al., (2007) (this volume) that includes our own solutions for the continuously recording BARGEN network (Wernicke et al., 2000; Bennett et al., 2003), and also the published and updated velocities from about a dozen campaign networks (see Table 1 of Kreemer et al., 2007 and references therein). The individual velocity solution sets are transformed so that they refer to the Stable North America Reference Frame (SNARF) (Blewitt et al., 2005). The resulting velocity field spans the majority of the Basin and Range province in California, Nevada, Utah, Arizona, Oregon and Idaho. The sites are shown in Figure 1, and the velocities are shown in Kreemer et al., (2007). While the velocity map has spatial density of sites that is highly variable (from <10s to 100s of kilometers), the coverage in the vicinity of the CNSB has at least a dozen sites within 30 km of every fault segment.

Interferometric Synthetic Aperture Radar (InSAR)

We use the InSAR results of Gourmelen and Amelung, (2005) that measure the change in range between the surface and a satellite in low Earth orbit over time. They stacked numerous interferograms constructed from repeat passes of the radar satellite over the CNSB in order to cancel noise and reduce the uncertainty in the rate of movement. They argue that most of the surface motion observed at the CNSB using this technique is attributable to vertical motion of the surface because the horizontal GPS signal in the same area (Hammond and Thatcher, 2004) cannot explain the InSAR data.

Thus the observations are most consistent with a dome-like uplift with a rate of 2-3 mm/yr centered over the Fairview Peak/Dixie Valley/Pleasant Valley ruptures. This uplift is not well observed in the GPS measurements because the uncertainties in the vertical component of GPS are a factor of 3-4 larger than in the horizontal, and exceed the signal observed by Gourmelen and Amelung (2005). Other GPS sites that are continuously recording, such as the BARGEN network (Bennett et al., 1998; Wernicke et al., 2000), or that have had significantly longer observation history, such as the Basin and Range Highway 50 network (Thatcher et al., 1999; Hammond and Thatcher, 2004) are not ideally positioned to observe the uplift seen with InSAR, since they lie to the south, east or west of the maximum of the bulge. Thus the InSAR measurements currently represent the best available source of relative vertical motion across the CNSB.

The U.S.G.S. Quaternary Fault and Fold Database

We use data from the USGS Quaternary Faults and Folds database in the Basin and Range and California (hereafter referred to as UQFD, Haller et al., 2002; Cao et al., 2003) to constrain the amount of permanent tectonic deformation that has occurred in the Basin and Range in the recent geologic past. A live internet accessable version of this database is available at http://earthquake.usgs.gov/qfaults/, but we used the specific tables associated with the Haller et al., (2002); and Cao et al., (2003) references. It contains a compilation of fault geometries in the United States and associated estimates of slip direction and rate when available. In addition we include results from the more recent study of paleoseismic slip rates for the CNSB (Bell et al., 2004) and the compilation of

dePolo and Anderson, (2000) who used a reconnaissance technique to estimate rates of slip on 45 normal faults in the Basin and Range. Since their technique tends to identify an upper bound to slip rate, and we used these rates whenever available, our inferred rates of geologic moment release may be similarly high. The information contained in these databases is complementary to geodetic data that measures contemporary surface deformation. The geodetic velocity field may include transients that are not representative of time-invariant (i.e. many times greater than a seismic cycle) behavior or permanent deformation. In contrast, paleoseismic data constrain the age, location and style of permanent surface deformation accommodated by slip on faults. If tectonic deformation progresses at a constant rate over time, then paleoseismology should constrain the same horizontal deformation field of the Earth surface that is measured by geodesy, when adjusted for transient effects.

The fault slip rate information is used to infer horizontal strain rates by using the moment tensor summation method of Shen-Tu et al., (1999), which is based on the approach of Kostrov, (1974). We create a map-view grid of the Basin and Range province with 0.4˚ x 0.4˚ horizontal two-dimensional cells. Inside each cell with area A, we calculate the average horizontal strain rate tensor by summing over n fault segments within the cell:

$$\dot{\varepsilon}_{ij} = \frac{1}{2}\sum_{k=1}^{n} \frac{L_k \dot{u}_k}{A \sin\delta_k} \, \dot{m}_{ij}^{k} \qquad (1)$$

where L_k is the length, δ_k is the fault dip angle, and $\dot{u}_k$ is the scalar slip rate of the *kth* fault. The unit moment tensor m_{ij}^{k} is defined as $m_{ij} = u_i n_j + u_j n_i$, where $\boldsymbol{n}$ is the horizontal unit vector normal to the fault trace, and $\boldsymbol{u}$ is the horizontal direction of slip across the

294 fault (Shen-Tu et al., 1998; Kreemer et al., 2000). The horizontal tensor strain rate for
295 each cell is obtained through the summation (1). The associated vector velocity field can
296 be obtained through integration of the strains plus definition of a reference frame. The
297 resulting map of permanent deformation associated with the fault database is shown in
298 Figure 2.

299 The resulting strain field obtained from the UQFD (Figure 2) is similar in spatial
300 pattern and deformation style to that obtained from the geodetic velocity field (method
301 discussed in Kreemer et al., 2007). Both have zones of more rapid deformation in the
302 westernmost 100-200 km of the Basin and Range. Both have zones of right lateral and
303 extensional slip and have velocities oriented west/northwest that increase and rotate
304 clockwise to the west. The similarity in these two deformation patterns suggests that the
305 geodetic velocity field is dominated by the time-invariant component of deformation.
306 There are, however, a number of differences in the details of the geologic and geodetic
307 models. For example, in general the geologic strain rates are considerably lower than the
308 geodetic rates. The differences between them may be partly attributable to
309 incompleteness of the catalog of surface faulting (which is spatially variable), and by the
310 presence of transients in the geodetic velocity field caused by postseismic relaxation.
311 Zones of higher rate deformation, associated with an east-west velocity gradient of 2-3
312 mm/yr are also located in the vicinity of the Wasatch Fault zone at the Great Basin
313 eastern boundary. Note that a small appendage of 4-8 nanostrains/yr strain rate seen in
314 the geologic strain rate map (Figure 2) near 117°W longitude and 39°N latitude is not
315 located at the CNSB, but southeast of it. The slightly higher strain rate in this band is
316 controlled by the proximity of several faults with <0.2 mm/yr slip rate estimates (Ione

317 Valley fault, Southwest Reese River Valley, Western Toiyabe Range) and one with 0.22
318 mm/yr (Toiyabe Range fault zone).

319 Differences between the geodetic and geologic deformation fields can, at least
320 partially, explained by the incompleteness of the geologic catalog of prehistoric
321 earthquakes. In a province-wide comparison of seismic, geologic, and geodetic moment
322 rates in the Basin and Range, Pancha et al., (2005) have shown that the rate of
323 geologically inferred moment release is less than that inferred from seismic and geodetic
324 moment rates. They estimated geodetic moment of between 4-7 x 10^{18} N·m/yr and
325 geologic moment of 2.5 x 10^{18} N·m/yr, implying a province-wide value for the ratio of
326 geodetic moment over geologic moment *R* between 1.6 and 2.8. We calculate our own
327 estimates of the ratio of geodetic over geologic moment rates *R* for each sub-domain
328 shown in Figure 1. To be consistent between out estimates of geodetic and geologic
329 moment, we calculate the average moment for each inside the 0.4˚ by 0.4˚ cells that cover
330 each of the regions defined in Figure 1 from the continuum strain rate models. We
331 assume that moment is proportional to the total strain rate defined as the second invariant
332 of the strain rates tensor (Kreemer et al., 2007) and then sum the moments in each region.
333 The Central Basin and Range (which includes the Wasatch), northern Walker Lane,
334 Yucca Mountain, Oregon and southern Walker Lane domains have *R*= 2.9, 4.9, 2.0, 3.9
335 and 3.9 respectively. For sites closest to the CNSB (within ~70 km) *R*=9.5 consistent
336 with the geodetic deformation exhibiting elevated strain rates via transient effects. For a
337 geographically broader selection of sites (within ~180 km) centered at the CNSB *R*=5.1
338 consistent with the presence of enhanced geodetic moment that is focused near the
339 CNSB.

340 The relatively high values of *R* for the northern and southern Walker Lane are
341 driven by geodetic strain rates that are highest at the westernmost boundary of the Basin
342 and Range, adjacent to the Sierra Nevada microplate (Kreemer et al., 2007). In this
343 version of the UQFD the Mohawk Valley fault is not present and thus effectively has a
344 rate of 0.0 mm/yr. It has been shown recently to have 0.3–0.5 mm/yr slip on a single
345 strand (Sawyer et al., 2005). Also in our version of the UQFD, the Owens Valley fault
346 has a rate of 1.5 mm/yr, which is now estimated in the current version of the database to
347 be 1.0–5.0 mm/yr (http://earthquake.usgs.gov/qfaults accessed March 2007). Thus it is
348 likely that values for *R* would be smaller for the southern and northern Walker Lane if
349 they were estimated from a more current UQFD database. The data are also consistent
350 with a province-wide moment rate deficit in the paleoseismic earthquake catalog, of an
351 approximate factor of 3±1, since areas without significant historic seismic moment
352 release also show a discrepancy.
353 Another difference between the geologic model (Figure 2) and the geodetic model
354 (Figure 3) of Kreemer et al., (2007) is seen in the azimuth of velocities in southern
355 Nevada, western Utah and northwest Arizona. In this area the geologic model velocities
356 have a southwest azimuth, where as the geodetic model velocities have an azimuth north
357 of west. However, in both models the tensor strain rates are the primary solution and
358 velocities are obtained by integrating the strains while defining the velocity reference
359 frame to be zero at the eastern edge of the model, east of the Wasatch fault zone in
360 eastern Utah and southwest Wyoming. Uncertainties in this zero velocity condition on
361 this boundary allow for a small solid body rotational difference in the velocity fields,
362 with a pole of rotation near the Wasatch. Adjusting for such a rotation could add a

363 northwest component to velocities in southern Nevada, giving them a more western
364 azimuth, without changing the fit to the geologic data. Furthermore, 1-3 mm/yr GPS
365 velocities in southern Nevada and on the Colorado Plateau have a west azimuth and drive
366 the azimuth in the geodetic model. No such constraint exists in the geologic model, since
367 the rates on the Hurricane in southwest UT and northwest AZ are very low, and strain
368 rates east of the Colorado Plateau are not taken into account. These differences,
369 however, do not affect the strain rate patterns in either figure.
370
371
372 **RELAXATION MODELING**
373
374 There are several lines of evidence that suggest that postseismic processes are
375 observable decades after the CNSB earthquakes, and that these are dominated by the
376 process of viscoelastic relaxation of the lower crust and/or upper mantle. These
377 arguments fall into three classes. First, observations of similar magnitude earthquakes
378 that have occurred during the era of modern geodetic observation have been used to infer
379 upper mantle and lower crustal viscosities of 10^{17} - 10^{21} Pa·s, and rule out other processes
380 such as poro-elastic rebound and afterslip (Pollitz et al., 2000; Pollitz et al., 2001; Hearn,
381 2003; Pollitz, 2003). Studies of other mid-20^{th} century Basin and Range earthquakes (e.g.
382 Borah Peak, and Hebgen Lake) (Nishimura and Thatcher, 2003; Chang and Smith, 2005)
383 and Lake Lahontan and Bonneville rebound (Bills and May, 1987; Bills et al., 1994;
384 Adams et al., 1999) have found similar values for lower crust/upper mantle viscosities
385 (Table 2). These suggest that the conditions for viscoelastic relaxation are present and

386 will have the decades-long time scale needed to provide a signal in the year 2005. Other
387 processes such as afterslip and poroelastic rebound are not expected to provide
388 observable signals so long after the earthquakes. Second, the CNSB exhibits a geodetic
389 signature that is consistent with the presence of ongoing viscoelastic relaxation. A broad
390 vertical uplift in the vicinity of the Dixie Valley/Fairview Peak and Pleasant Valley
391 ruptures has been observed using stacks of InSAR scenes (Gourmelen and Amelung,
392 2005). This horizontal dimension and vertical rate, and decades-long relaxation time-
393 scale of this broad bulge are consistent with viscosities obtained in other studies.
394 Horizontal GPS measurements reveal anomalous dilatation at the CNSB which is
395 consistent with this bulge (Hammond and Thatcher, 2004; Kreemer et al., 2007), and
396 contractions east of the CNSB that are otherwise difficult to reconcile with a region that
397 is undergoing tectonic extension, have been tentatively identified (Wernicke et al., 2000;
398 Bennett et al., 2003; Friedrich et al., 2004; Hammond and Thatcher, 2004). Thirdly, the
399 disagreement between geodetic and geologic slip and moment rates is large in the vicinity
400 of the CNSB (R=5.1 – 9.5) and southern Walker Lane domains (R=3.9), which contain
401 the large historic earthquakes, compared to the adjacent domains. These large R values
402 can be explained by an enhancement of geodetic strain resulting from viscoelastic
403 relaxation. This argument alone is only consistent with relaxation rather than proof of it,
404 however, since regions that have undergone less paleoseismic investigation can have
405 relatively incomplete moment derived from the UQFD.
406
407 **Modeling: Philosophy and Construction**
408

409 Considering the above arguments we proceed under the assumption that transient
410 deformation in the geodetic signal is caused by viscoelastic postseismic relaxation of the
411 lower crust and upper mantle. However, measurements of the geodetic velocity field at
412 the surface of the Earth capture effects related to both time-invariant and transient
413 processes that are a direct manifestation of the earthquake cycle. The transient effects
414 can be related to the observed geodetic velocities via

415 $$v_{\text{geodesy}} = v_{\text{time-invariant}} + v_{\text{transient}} \qquad (2)$$

416 where we constrain v_{geodesy} with GPS and InSAR observations and constrain $v_{\text{transient}}$ with
417 the physics governing viscoelastic deformation of a layered medium. Equation (2) can
418 also be expressed in terms of the spatial derivatives of velocity, i.e. strain rates, which we
419 use in the criteria for model fit that we present below. We consider the time-invariant
420 component of the geodetic velocity field as an unknown, and model the transient portion
421 of the velocity field by assuming a layered viscoelastic structure that is stressed by the
422 CNSB earthquake dislocations given in Table 1. Thus for each viscosity structure there
423 is an associated postseismic transient velocity field, and an associated time-invariant
424 velocity field derived from (2).

425 To model the evolution of the relaxation following the seismic events, we use the
426 spherically layered viscoelastic modeling software VISCO1D (Pollitz, 1997). The
427 software assumes a Newtonian Maxwell viscoelastic rheology and includes the effects of
428 gravitation which can have minor effects on the relaxation history at long times after the
429 earthquake. Because we assume Newtonian rheology, we may sum the independently
430 modeled earthquakes responses in the year 2005 to get the combined response. Although
431 some studies have suggested that power-law, bi-viscous or transient rheologies are

needed to explain the postseismic response, these studies are usually based on data obtained within days to a few years after the earthquake (Pollitz et al., 2001; Pollitz, 2003; Freed and Burgmann, 2004), when multiple processes may have contributed to the postseismic response (Fialko, 2004). The Maxwell Newtonian rheology is simpler and is usually an adequate explanation of the data on time scales of 10,000-15,000 years (e.g. Bills et al., 1994; Adams et al., 1999; Hetland and Hager, 2003; Nishimura and Thatcher, 2003; Pollitz et al., 2004). Furthermore, we expect that the mechanisms that have shorter relaxation times (e.g. poroelastic rebound (Fialko, 2004)) will have dissipated early in the decades between the time of the GPS measurements and the events we consider. Based on previous structural and dynamic studies, we assume a laterally homogeneous 15-km thick elastic uppermost layer that represents the upper crust, overlying a 15-km thick viscoelastic lower crust (Figure 3). This structure is a simplification based on studies that suggest a flat seismic Moho at 30-35 km depth (e.g. Allmendinger et al., 1987; Benz et al., 1990; Holbrook, 1990; Gilbert and Sheehan, 2004), and a rheological distinction between the lower and upper crust (see references in Table 2). The viscoelastic upper mantle extends from the bottom of the lower crust to a depth of 370 km. We tested models having a deeper bottom to the viscoelastic upper mantle (down to a depth of 1088 km), and these gave nearly identical relaxation velocities (difference less than 0.1 mm/yr). The values for the shear and bulk elastic moduli are from the global one-dimensional seismic model PREM (Dziewonski and Anderson, 1981) mapped into discrete layers 2 – 35 km thick, thickening with depth. The values for the viscosity of the lower crustal and upper mantle layers are iteratively selected in a grid search, varying each from 10^{17} to 10^{21} Pa·s in logarithmic steps of one half order of magnitude. For each

455 model, the velocities in the year 2005 at each of the GPS sites shown in Figure 1 is
456 computed, and include the combined effects of each of the earthquakes listed in Table 1.
457 We use the characteristics of both the transient and time-invariant velocity fields
458 to constrain the viscosities of the lower crust and upper mantle. To achieve this we apply
459 three objective criteria for the elimination of models that violate one or more of our three
460 sources of data: GPS, InSAR, and paleoseismology. We cannot simply compare the
461 results of our calculations to the geodetic observations because only the transient
462 component of the velocity field is obtained in the viscoelastic modeling. Instead we use
463 the transient model and the observed GPS velocities to estimate the long-term velocity
464 field using equation (2), and then select a best model based on a synthesis of all of the
465 following three objective, and independent, criteria:
466 1) The inferred time-invariant velocities in the vicinity of the CNSB must imply a
467 moment accumulation rate that makes a better match to the geologic moment release rate
468 than do the raw GPS velocities. This criteria is based on the assumption that the
469 mismatch between geodetic and geologic moment rates can be explained, at least in part,
470 by the presence of postseismic viscoelastic relaxation.
471 2) The transient model must predict the uplift that is observed with InSAR. The
472 vertical contribution from the time-invariant motion is presumed to be negligible at the
473 CNSB. This is consistent with slip rates, constrained by paleoseismology, that have an
474 extensional component of slip that is less than 0.7 mm/yr total for four faults crossed by
475 U.S. Highway 50 and less than 0.3 mm/yr for each of them, (Bell et al., 2004). However,
476 the observed motion is 2-3 mm/yr of surface uplift (Gourmelen and Amelung, 2005), at
477 least several times greater than is expected based strain accumulation. The wavelength of

deformation expected from the transient response (>100 km) is much broader and is theoretically separable from the elastic strain response of individual faults (a few tens of km). Thus the spatial characteristics of the two processes could be used to separate the vertical component of the relaxation signal. However that work is beyond the scope of this study, and we here assume that all the vertical signal is attributable to relaxation.

3) The time-invariant model must not predict long-term contraction in regions characterized geologically by tectonic transtension. This is identical to, but more generally applied than, the assumption used by Hetland and Hager, (2003) in an analysis of the horizontal GPS data of Thatcher et al., (1999) and Wernicke et al., (2000), where they assumed that contraction east of the CNSB needed to be explained by the postseismic model.

These criteria can be more generally applied to tectonically deforming areas that have experienced recent earthquakes that may be affecting the modern geodetic velocity field. Also notice that none of these criteria require that the postseismic deformation field resemble the time-invariant velocity field in pattern, style or rate. For the CNSB, the above criteria select a clearly defined best model, as described below.

Resolving Power of GPS, InSAR and Geologic Data

The InSAR and horizontal GPS velocities form highly complementary constraints on the upper mantle and lower crustal viscoelastic structures. Each data type excludes very different portions of the model space. To evaluate the misfit of the viscosity models

500 to the different types of data, we design the misfit as the combination of three different
501 terms

502 $$\chi^2 = \alpha(R-1)^2 + \left(\frac{v_u - v_{InSAR}}{\sigma_{vu}}\right)^2 + \sum_{i=1}^{6}\left(\frac{\varepsilon_\Delta}{\sigma_{\varepsilon\Delta}}\right)^2 \qquad (3)$$

503 were R is the ratio of geodetic moment to geologic moment estimated in the CNSB
504 domain, v_u is the maximum vertical velocity in the CNSB domain obtained for each
505 model in the grid search. The quantities v_{InSAR} and σ_{vu} are the vertical rate and its
506 uncertainty observed with InSAR at the CNSB taken to be 2.5±0.5 mm/yr (Gourmelen
507 and Amelung, 2005). The dilatational strain rate ε_Δ and its uncertainty $\sigma_{\varepsilon\Delta}$ are obtained
508 from the estimated time-invariant velocity field and the formal uncertainty obtained in the
509 strain rate calculation. For the purposes of calculating the misfit, we assign $\varepsilon_\Delta=0$
510 whenever $\varepsilon_\Delta>0$ so that no extensional deformation, regardless of its rate, will be
511 penalized. The summation in the third term sums the contributions from each of the
512 domains. The Oregon domain is not included because contractions owing to Cascadia
513 interseismic strain accumulation (McCaffrey et al., 2000; Miller et al., 2001b; Svarc et
514 al., 2002a) and from the collision of the Sierra Nevada microplate with the Oregon
515 domain (Hammond and Thatcher, 2005) are likely present and should not be penalized.
516 The resulting misfit surfaces, for each of the terms in (3) and for the combined constraint,
517 are shown in Figure 6. The weight α is applied to control the relative importance of the
518 first term, since it is not normalized by an uncertainty. We begin with a trial value of
519 $\alpha=1$, and then reduce α until models that are excluded by any single criterion are still
520 excluded by the combined criteria, arriving at $\alpha=0.7$. In other words, dark regions in
521 Figure 6abc are also dark in Figure 6d. This approach gives approximately equal model

exclusion power to the first term compared to the second and third terms in (3). The minimum misfit taking all three criteria into account (Figure 6d) identifies $\eta_{LC}=10^{20.5}$ and $\eta_{UM}=10^{19}$ as the best fitting model. This result appears to agree well with each of the individual criteria, since this model lies inside the region of minimal geologic/geodetic, InSAR, and contraction constraint misfit (Figures 6a-c). Models that fit similarly well can be found by decreasing η_{LC} and/or η_{UM} by one half order of magnitude, but outside the zone defined by the contour where $\chi^2=2$ misfits increase rapidly. The misfit in the InSAR term increases most rapidly when η_{UM} is above 10^{19} Pa·s or reduced below $10^{18.5}$ Pa·s. When η_{LC} is decreased the InSAR constraint yields a greater misfit, however a more powerful limit on the lower bound of η_{LC} comes from the introduction of time-invariant contractions in the Sierra Nevada and CNSB domains when η_{LC} is below 10^{20} Pa·s. The lower crustal viscosity η_{LC} could be greater than $10^{20.5}$ and not strongly violate the InSAR result, but would come at some cost to the fit between geologic and geodetic data. The precise amount of uncertainty in the estimates of η_{LC} and η_{UM} is difficult to quantify because (3) is not a truly normalized measure of model misfit and α is subjectively assigned. However, the models outside the $\chi^2=4$ combined constraint contour in Figure 6d are being excluded by at least one of the criteria. Thus uncertainties in η_{LC} and η_{UM} are near one half order of magnitude.

Results

To guide the evaluation of our results, the sites have been divided into separate geographic domains so that different regions can be evaluated individually. These

545 domains are 1) the southern Walker Lane, 2) the northern Walker Lane, 3) the Sierra
546 Nevada microplate, 4) the CNSB, 5) southern Oregon, 6) the eastern Basin and Range
547 and 7) the Yucca Mountain area (Figure 1). These domains have been selected,
548 somewhat subjectively, according to their first order deformation characteristics based on
549 previous geodetic and geological studies. For each viscoelastic model we calculate the
550 horizontal tensor strain rate inside each of the sub-domains from the estimated time-
551 invariant velocity field. We estimate the three horizontal strain rate parameters ($\varepsilon_{\phi\phi}$, $\varepsilon_{\lambda\lambda}$,
552 $\varepsilon_{\phi\lambda}$) simultaneously with three solid body rotation parameters (latitude λ, longitude ϕ, and
553 rotation rate ω) on the surface of a sphere according to the method of Savage et al.,
554 (2001)]. Figure 4a shows the dilatational component of the strain rate ε_{Δ} calculated for
555 sites inside the CNSB domain and corrected for the effects of postseismic relaxation
556 based on each of the models in our grid search. The strain rate has been normalized by
557 its uncertainty to illustrate the transition to models that imply no significant deformation
558 in the CNSB domain.

559 In order to evaluate the models according to our first objective criterion, we
560 examine the ratio of geodetic moment rate corrected for postseismic effects to geologic
561 moment rate in the CNSB domain. The geologic moment is obtained from the UQFD
562 and (1), while the geodetic moment is obtained from the GPS velocities corrected for
563 postseismic effects via the relaxation models. The modified ratio *R* is shown as a
564 function of model viscosities in Figure 4b. Because the UQFD is not everywhere
565 complete we have speculated that there is a background disagreement rate between
566 geodetic and geologic moment rates of a factor of 3±1, which is near the lowest value for
567 modified *R* Figure 4b. This assertion assumes, however, that the database is equally

568 incomplete at all locations in the Basin and Range, and hence that the anomalously high
569 ratio in the CNSB is not the result of systematically less complete geologic record. In
570 fact it is more likely that the opposite is true since the CNSB has been the focus of
571 numerous studies owing to its vigorous historic seismicity and proximity to the
572 Reno/Carson Metropolitan area. In Figure 4b, lower values for modified *R* occur in a
573 part of the model space that has intermediate values for lower crust viscosity η_{LC} ($10^{18.5}$ –
574 $10^{20.5}$ Pa·s) and intermediate to high values for upper mantle viscosity η_{UM} (>$10^{18.5}$ Pa·s),
575 with the highest values for η_{UM} if η_{LC} is in a narrower band ($10^{18.5}$ – $10^{19.5}$ Pa·s). The
576 lowest values for modified *R* are near the speculated background level, and hence models
577 inside the light central region of Figure 4b are more likely to be correct models according
578 to the first objective criteria. The similarity between Figures 4a and 4b suggests that the
579 misfit between geodetic and geologic moment rates is controlled by the dilatational
580 component of the geodetic strain rate field in the vicinity of the CNSB. This is consistent
581 with the observation of anomalously high geodetic dilatation at the CNSB (Savage et al.,
582 1995; Svarc et al., 2002b; Hammond and Thatcher, 2004) and the likely presence of
583 dilatation in the postseismic deformation that follows earthquakes with a normal
584 component of slip (i.e. Pleasant Valley and Dixie Valley).

585 The second objective criterion eliminates viscosity models based on misfit
586 between the vertical motion observed with InSAR and that predicted by the relaxation
587 calculations. The maximum vertical velocity inside the CNSB domain as a function of
588 the viscosity model is shown in Figure 5. It is immediately clear that the only models
589 that can produce a >2 mm/yr uplift are those with a relatively high lower crustal viscosity
590 (η_{LC}>10^{20} Pa·s), and an intermediate upper mantle viscosity (η_{UM} between $10^{18.5}$ and 10^{19}

591 Pa·s). The range of viscosities that are eliminated by this criterion is very large, and is
592 complimentary to that of models eliminated by the geologic/geodetic misfit, i.e. the
593 overlap between regions of acceptable fit in Figure 4 and Figure 5 is small. What
594 constitutes an acceptable fit will be discussed below.

595 The Basin and Range is characterized by (oblique) normal faulting, so the third
596 objective criterion is designed to eliminate models that predict time-invariant
597 contractions, in violation of geological observation. The minimum and maximum time-
598 invariant dilatational strain rates ε_Δ as a function of the viscosity model for each domain
599 are shown in Table 3. None of the ε_Δ has a normalized value below –2, which would
600 indicate a contraction rate that has exceeded the two-sigma uncertainty level. Only the
601 Oregon domain exhibits a normalized contraction below –1, which indicates there may be
602 some contraction of the entire domain. This is consistent is with the presence of
603 interseismic strain accumulation that is expected in the Cascadia backarc (McCaffrey et
604 al., 2000; Miller et al., 2001b; Svarc et al., 2002a) and also with a north-south contraction
605 of 2-3 mm/yr observed near the Oregon/California border (Hammond and Thatcher,
606 2004). The minimum and maximum ε_Δ in Table 3 also provide an illustration of the
607 sensitivity of strain rate field to the viscoelastic properties of the lower crust and upper
608 mantle. The range between the maximum and minimum ε_Δ is greatest for the CNSB
609 domain, consistent with its location near the historic earthquakes. The northern Walker
610 Lane domain sees a transition from marginally insignificant to marginally significant
611 dilatation. This implies that geodetic results that show no dilatation (e.g. Hammond et
612 al., 2004) may have been influenced by the presence of relaxation, which can mask a
613 small amount of secular extension. This is discussed more completely below.

614 Table 4 shows that correcting the geodetic strain rate field with this model makes
615 the deformation more similar to the geologic strain rate field with respect to geographic
616 distribution of strain rate style, if not with respect to the total magnitude of strain (which
617 are a factor of 2-5 smaller for the geologic model). The table shows a comparison
618 between the strain rates inside the separate regions calculated from the geodetic strain
619 rate model velocities, geologic data via the UQFD and equation (1), and from the
620 postseismic model. This table shows the similarity between the geologic and geodetic
621 datasets with respect to the dominance of shear strain in western Basin and Range
622 Province, particularly the southern Walker Lane, northern Walker Lane and Yucca
623 Mountain regions. The only region which shows significant geodetic dilatation is the
624 CNSB, in contrast to the geologic model which shows generally less dilatation than shear
625 everywhere. A property of the postseismic relaxation model is that all the dilatation and
626 most of the shear focused at the CNSB, consistent with it being the locus of the historic
627 earthquakes used in its construction. Thus the geodetic strains minus the postseismic
628 relaxation model will have much less dilatation, similar to the geologic model. Note that
629 the geodetic minus the correction will not match the geologic model exactly, because of
630 the province-wide lower magnitude of deformation rate seen in the geologic data.
631 However the corrected geodetic strains provide a model that is similar to the geologic
632 model in the sense that most dilatation has been removed, and shear strain rates at the
633 CNSB are lower than in the Walker Lane. The very strong correlation between R and the
634 dilatational component of the relaxation model suggests that the model has been
635 appropriately built to compensate for the anomalous dilatation at the CNSB.
636

DISCUSSION

Implications for Time-invariant Deformation of the Northern Walker Lane

The postseismic strain rates predicted by our preferred viscosity model are obtained from the postseismic velocity field obtained from the relaxation calculations. The velocities predicted from our preferred model (Figure 7 and Table 4 in the online data repository) are consistent with northwest-southeast uniaxial extension across Pleasant Valley, and significant vertical uplift of ~2 mm/yr predicted north of the Fairview Peak rupture. To the south, progressively greater amounts of shear deformation appear where the style of the earthquakes became more strike-slip. The dilatational component of postseismic transient strain rate (Figure 8a) shows enhanced extension in the vicinity of the CNSB. This patch of dilatation is spatially coincident with the anomalously high CNSB dilatation rates shown in the strain rate map in a companion article to this paper (Kreemer et al., 2007). This dilatation comes mostly in the form of uniaxial northwest-southeast directed extension, and is visible in the detail that includes the strain rate tensor axes (Figure 8b). The relaxation model also contains lobes of low-intensity (1-4 nanostrain/yr) contraction to the northwest and east of the CNSB historic ruptures. The lobe to the east is consistent with GPS observations of geographically broad contraction east of the CNSB (Hammond and Thatcher, 2004), but do not explain a narrow zone of contraction inferred from the single continuous GPS site LEWI on Mt. Lewis NV, near Crescent Valley (Wernicke et al., 2000; Bennett et al., 2003; Friedrich et al., 2004). The significant east-west asymmetry in these contractional lobes comes from

660 summing earthquakes with different strikes, event times, and different ruptures styles.
661 Shorter wavelength variations are mainly the result of geographic irregularity in the GPS
662 sites, which causes irregular sampling of the model relaxation velocity field that is used
663 in the strain modeling. For example, near the Owens Valley rupture at the southern end
664 of our model, small blotches of dilatation of alternating sign exist, but contribute
665 negligibly to the integrated dilatation over larger regions. The transition of tensor
666 deformation style from south to north (Figure 8b) can also be seen in the model velocities
667 (Figure 7). Where the earthquake styles to the south have a larger component of right
668 lateral slip, we see postseismic deformation that has close to equal parts of contraction
669 and extension, indicating shear deformation. To the north, near the Pleasant Valley
670 rupture, the style of extension is closer to northwest-southeast uniaxial extension, similar
671 to the coseismic rupture there. In the vicinity of Pyramid Lake, roughly 2-4 nanostrain/yr
672 of northwest directed uniaxial contraction is predicted from the relaxation model.
673 The time-invariant deformation field is estimated by subtracting the transient
674 velocities from the GPS velocities and then repeating the strain rate modeling of Kreemer
675 et al., (2007). Thus the strain rate map of Figure 9b is expected to be in closer agreement
676 to the deformations inferred from paleoseismological studies. A comparison of Figure 2
677 and Figure 9b shows that this is the case, since deformation in the time-invariant model
678 and in the geologic model is more strongly focused into the Northern Walker Lane, and
679 has relatively little deformation at the CNSB. A single small zone of strain near
680 longitude 118.5˚W, latitude 40˚N is caused by a single campaign GPS velocity (site
681 WILD) that has a velocity that deviates by ~1 mm/yr from the smooth regional pattern.
682 The finger of higher geologic strain rate near longitude 117˚W, latitude 39˚N and the

683 Toiyabe Range (Figure 2), is not observed in the uncorrected or corrected geodetic strain
684 rate models (Figure 9). It likely shows higher moment rate because of the close
685 proximity of the Toiyabe Range Fault (0.22 mm/yr), the Ione Valley Fault (0.1 mm/yr),
686 the Southwest Reese River Valley Fault (0.1 mm/yr), and the Mahogany Mountain
687 section of the Western Toiyabe Range fault zone (0.2 mm/yr).

688 After correction for postseismic effects, some deformation at the CNSB remains,
689 with rates that are still higher with respect to the eastern Basin and Range (Figure 9b). In
690 the vicinity of the Stillwater, Dixie Valley, and Fairview Peak faults, the total strain rates
691 are 8-32 nanostrain/yr, and a bit lower near Pleasant Valley. Near the Cedar Mountain
692 rupture, strain rates are higher, 16-32 nanostrain/yr, reduced from the 32-64 nanostrain/yr
693 estimated before the correction. The velocity gradient across the CNSB (between sites
694 B220 and B290, Figure 1) is 3.1 mm/yr in the GPS velocity compilation, but has been
695 reduced to 0.9 mm/yr in the time-invariant model. Thus, a significant fraction of the
696 deformation at the CNSB has been explained with postseismic relaxation, yet some
697 remains and is consistent with the paleoseismological result of ~1 mm/yr extension
698 across the CNSB faults (Bell et al., 2004). The amount of velocity gradient that still
699 exists across the CNSB after the correction indicates the CNSB may still be a zone whose
700 rate of deformation is greater than in the Central Basin and Range, where strain rates are
701 close to zero (Bennett et al., 2003; Kreemer et al., 2007). The corrected rates are,
702 however, less than what is observed in the Walker Lane to the west. Thus, these results
703 are consistent with a greater frequency of paleoearthquakes at the CNSB compared to the
704 central Basin and Range, and the view that the CNSB is a zone of deformation that
705 extends to the northeast possibly transferring Walker Lane dextral slip onto NNE striking

706 normal faults (Wesnousky et al., 2005; Faulds et al., 2005). For GPS sites further north
707 and farther apart that span Pleasant Valley, the difference owing to the correction is not
708 as large. The relative velocity of GARL and D100 changes from 2.3 mm/yr to 1.3 mm/yr
709 upon adjusting for postseismic deformation. In general the magnitude of the correction
710 decreases with distance from the CNSB.

711 The time-invariant dilatation rate in the Northern Walker Lane domain is 8.8±3.9
712 nanostrains/yr (Table 3), just barely significant to 95% confidence, while its shear strain
713 rate is 33.8±3.9 nanostrains/yr (shear is defined as $\varepsilon_1 - \varepsilon_2$, where ε_1 and ε_2 are the
714 maximum and minimum principal strain rates, respectively). This suggests that, as a
715 whole, the northern Walker Lane acts as a right lateral shear zone with a small
716 component of extension. However, this extension becomes statistically significant only
717 after the correction for postseismic relaxation from the CNSB historic earthquakes has
718 been made. Thus in several respects, the northern Walker Lane behaves similarly to the
719 central Walker Lane where dextral shear rates are greater than extension rates, and the
720 highest deformation rates are seen near the western boundary of the Walker Lane
721 adjacent to the Sierra Nevada (Oldow et al., 2001; Oldow, 2003). Furthermore, these
722 observations are consistent with campaign GPS data spanning the Walker Lane between
723 37°-40° N, that saw significant extension approximately normal to the trend of the shear
724 zone, but changed orientation from east to west (Oldow, 2003; Hammond and Thatcher,
725 2004). It is also consistent with the results of a profile of campaign GPS velocities across
726 the northern Walker Lane in the vicinity of Pyramid Lake (Hammond et al., 2004) that
727 did not correct for postseismic relaxation, and observed no significant dilatation.
728

729 **Implications for Basin and Range Lithospheric Rheology**

730

731 The conclusions reached here are broadly consistent with Basin and Range lower
732 crustal and upper mantle viscosity estimates from a number of other studies. We have
733 summarized the values obtained by a sample of other studies in Table 2. The most
734 common conclusion reached for the Basin and Range is that the lower crust has greater
735 strength (i.e. higher viscosity) than the uppermost mantle on which it lies. This
736 conclusion is consistent across studies that sample a great variety of temporal scales,
737 from times immediately following (<3 years) an earthquake (Pollitz et al., 2000; Pollitz et
738 al., 2001; Pollitz, 2003), to over 10,000 years of relaxation following the unloading
739 owing to the draining of late Pleistocene post-glacial lakes (e.g. Nakiboglu and Lambeck,
740 1983; Bills and May, 1987; Bills et al., 1994; Kaufmann and Amelung, 2000).
741 In their study of CNSB rheological layering, Hetland and Hager, (2003) relied on
742 the criterion that time-invariant contraction should be explained by postseismic
743 relaxation. Our modeling differs from theirs because we choose to exclude models that
744 predict time-invariant contractions in any of the domains near the CNSB. We do not
745 explain the contraction east of the CNSB directly, because we do not observe the
746 contraction in our Central Basin and Range domain. This is likely owing to the fact that
747 our domain is so large and also includes the Wasatch fault zone to the east. However,
748 when we use just the criterion that Central Basin and Range domain extension should be
749 positive, amounting to approximately the same model discrimination criterion that they
750 use, we would have estimated that the $\eta_{LC} \approx 10^{19}$ and that $\eta_{UM} \geq \eta_{LC}$, very similar to their
751 results. Their reliance on this criterion may explain why their result is the only one of the

752 survey of previous results (Table 2) that indicate a lower crust that is weaker than the
753 upper mantle.

754 Our results, and most of the results listed in Table 2 appear to be in disagreement
755 with the results of others that suggest that the lower crust behaves as a low viscosity
756 channel through which material flows. Sometimes called the "jelly sandwich" model
757 (Jackson, 2002), this idea has been used to explain the scarcity of earthquakes in the
758 lower crust, the existence of metamorphic core complexes (e.g. Block and Royden,
759 1990), and the flatness of Moho topography despite geologic extension that is, at the
760 surface, localized to dipping normal faults and heterogeneous over scales of 100s of
761 kilometers (Gans, 1987). The geodetic networks considered in this study are
762 geographically focused in the western Great Basin, where strain rates are 1-2 orders of
763 magnitude higher and metamorphic core complexes are absent. Thus variations in crust
764 and mantle properties may partially account for the discrepancy. However, results from
765 several studies in the eastern Great Basin (i.e. in the vicinity of Lakes Bonneville, Mead
766 and Hebgen) show no strong difference in η_{LC} compared to the western Great Basin (e.g.
767 CNSB, Walker Lane or Mohave Desert) (Table 2). According to the two-layer theory of
768 McKenzie et al., (2000), short wavelength Moho relief is flattened on a time scale that is
769 proportional to the sum of crust and upper mantle viscosities. Thus, it is possible to
770 flatten Moho topography if the crust is stronger than the mantle, as long as the crust is
771 weak enough to allow flow on the timescale of Basin and Range extension. For example,
772 in the two-layer viscous model with upper layer $10^{20.5}$ Pa·s over a half-space of 10^{19} Pa·s
773 (values of η_{LC} and η_{LC} in our preferred model), 10 km wavelength Moho topography will
774 relax with a characteristic decay time of 2.6 million years. This is short enough to flatten

775 Moho topography over the history of Basin and Range extension, and thus weak lower
776 crust (compared to the mantle) is not an absolute requirement to flatten Moho
777 topography. Thus our model is not in conflict with the observation of a flat Moho.
778 An additional possibility is that lateral contrasts of lithospheric viscosity exist that
779 can affect our results and comparisons between the CNSB and other parts of the Basin
780 and Range. Modeling of the stresses driving deformation of the western United States in
781 the context of a thin viscous sheet suggests that the focused deformation in the
782 westernmost part of the province is attributable to lithosphere that has a lower viscosity
783 compared to the adjacent areas (Flesch et al., 2000). East-west asymmetry in lithospheric
784 effective viscosity is consistent with the presence of higher heat flow (Lachenbruch and
785 Sass, 1978; Blackwell and Steele, 1992), and lower flexural rigidity to the west (Lowry
786 and Smith, 1995). In this study we assumed a laterally constant viscosity, and thus our
787 modeling does not include the effects of east-west asymmetry in the relaxation velocity
788 field that would be expected from an increase in viscosity east of the CNSB. This can
789 affect the strain rates that are expected from the relaxation model far from the CNSB.
790 For example, our preferred model predicts some deformation in the southern Sierra
791 Nevada microplate (Figure 8a), which to date has not been definitively observed. Future
792 modeling studies will have to be undertaken to understand the effect of postseismic
793 relaxation in the presence of lateral variations in the strength of the Basin and Range
794 lithosphere.
795 Transient or power-law rheology in the upper mantle may explain relaxations that
796 occur more quickly immediately following a large earthquake than would be expected
797 from the longer term (>1 year) response assuming a Newtonian Maxwell viscoelastic

798 model (Pollitz, 2003; Freed and Burgmann, 2004). Our study assumes a linear response
799 and hence the velocity fields from the individual earthquakes can be modeled separately,
800 and then summed to represent the velocity field in the year 2005. A rheology other than
801 Newtonian violates this assumption. If, however, the mantle were characterized with a
802 power-law rheology that increased the inferred viscosity over time, as has been observed
803 in the Mojave (Pollitz et al., 2001; Pollitz, 2003), then our results would tend to
804 overestimate mantle viscosity, and our conclusions about the relative strength between
805 the crust and upper mantle would still hold. Similarly, if the viscosity is temperature
806 dependent, and hence smoothly decreases with depth, our modeling would be most
807 sensitive to the upper portion of each depth interval. This would result in a systematic
808 over-estimation of the viscosity in each layer, but would not alter the relative strength of
809 the lower crust and upper mantle.
810
811 **SUMMARY AND CONCLUSIONS**
812
813 We combine horizontal GPS velocities, InSAR and paleoseismic data with
814 modeling of the viscoelastic postseismic response of the CNSB historic earthquakes to
815 estimate the most likely viscoelastic structure of the western Basin and Range lower crust
816 and upper mantle. From these we develop a correction for postseismic effects that can be
817 used to estimate secular crustal deformation from geodetic velocities near the CNSB.
818 Our preferred model has $\eta_{LC}=10^{20.5}$ Pa·s and $\eta_{UM}=10^{19}$ Pa·s. To obtain this result we
819 assumed that the GPS velocity field is the sum of time-invariant and transient processes,
820 and seek models that 1) explain the mismatch between geodetic and geologically inferred

821 slip rates, 2) explain the vertical uplift that has been observed with InSAR and 3) do not
822 imply time-invariant contractions anywhere in the Basin and Range. This model is
823 consistent with other geodetic studies of earthquakes and lake loading of the lithosphere,
824 and with the observation of flat Moho topography throughout much of the Basin and
825 Range.

826 We evaluate the ability that different types of data have to constrain the
827 viscoelastic structure. We find that InSAR, GPS and geologic data exclude different
828 parts of the model space and thus form complementary constraints on the viscoelastic
829 structure. This suggests that studies that aim to constrain rheology of the lithosphere are
830 best served by using techniques that measure both vertical and horizontal movements,
831 plus include geologic constraints on steady permanent tectonic deformation averaged
832 over many seismic cycles.

833 The preferred viscosity model implies that the majority of the deformation
834 observed at the CNSB is attributable to postseismic relaxation, and that the time-invariant
835 deformation is more tightly focused into Northern Walker Lane than is inferred from the
836 uncorrected GPS velocities. Whereas no significant dilatation was detectable before
837 correcting for postseismic effects, following the correction the dilatation is significant
838 (8.4±3.9 nanostrains/yr). Thus the CNSB postseismic relaxation masks time-invariant
839 extension in the adjacent province to the west.

840 The preferred model decreases the apparent discrepancy between geologically and
841 geodetically estimates slip rates on faults at the CNSB. After using this model to correct
842 the geodetic velocity field for transient postseismic effects from this historic earthquakes,
843 the amount of geodetically inferred steady permanent extension that occurred at the

CNSB is reduced, making it less anomalous with respect to the Central Basin and Range, in agreement with paleoseismic data. However, after the correction rates of deformation at the CNSB are still greater than rates in the central Basin and Range to the east, and not as great as rates in the Walker Lane to the west.

ACKNOWLEDGEMENTS

The work was supported by the Department of Energy Geothermal Program through the Great Basin Center for Geothermal Energy, the Department of Energy Yucca Mountain Project, and in part by the State of Nevada. Special thanks to Fred Pollitz for sharing his VISCO1D software and assisting us with installation. We are grateful to all who contribute to and maintain the U.S.G.S. Quaternary Fault and Fold paleoseismic database. This manuscript was improved by careful reviews from Dennis Harry and Criag Jones.

857
858 **FIGURE CAPTIONS**
859

860 Figure 1. GPS sites whose horizontal velocities are used to constrain the viscosity of the
861 Basin and Range lower crust and upper mantle. Site color designates the strain rate sub-
862 network discussed in text. Magenta line segments are the fault segments used to model
863 the postseismic relaxation from the CNSB historic earthquakes. See text for details of
864 fault segments and coseismic slip parameters. Sites labeled GARL, B220, B290 and
865 D100 and having black interiors are discussed in the text. Fault segments are: CM, Cedar
866 Mountain; DV, Dixie Valley; GK, Gold King-Louderback sequence; FP, Fairview Peak;
867 OV, Owens Valley; PV, Pleasant Valley; SW, Stillwater sequence.
868

869 Figure 2. Strain rate field inferred from the paleoseismic databases of the U.S.G.S. and
870 dePolo and Anderson, (2000). Black arrows are velocities with respect to North America
871 on a regular grid that result from integration of the strain rates. Colors are the second
872 invariant of the strain rate (includes shear and dilatation). Magenta line traces are faults
873 in the database. Note that the finger of higher strain rates near longitude –117°, 39°N lies
874 east of the CNSB.
875

876 Figure 3. Rheological properties of our model as a function of depth. The uppermost
877 layer (0 – 15 km) is assumed to be elastic, the lower crust (15 - 30 km) and upper mantle
878 are assumed to be Maxwell viscoelastic. The elastic modulus μ is obtained from the one-
879 dimensional seismic model PREM (Dziewonski and Anderson, 1981), and viscosities of
880 the lower crust η_{LC} and upper mantle η_{UM} are varied in a grid search.

881

882 Figure 4. a) Contour of the dilatational strain rate after correction for postseismic
883 relaxation at the CNSB normalized by its uncertainty as a function of lower crustal (η_{LC})
884 and upper mantle (η_{UM}) viscosity. Values greater than 2 indicate dilatation that is
885 significantly larger than zero to 95% confidence. b) Contour plot of *R*, the ratio of the
886 scalar geodetic moment rate after correction for postseismic relaxation to the scalar
887 geologic moment rate in the CNSB.

888

889 Figure 5. Contour of uplift rate at the CNSB predicted from the relaxation model as a
890 function of lower crustal (η_{LC}) and upper mantle (η_{UM}) viscosity.

891

892 Figure 6. Model misfits as a function of lower crustal (η_{LC}) and upper mantle (η_{UM})
893 viscosity. a) Contour of the first term of (3) which depends on the ratio between geodetic
894 and geologic scalar moment rate. Lower values indicate a better match between geologic
895 and geodetic data. b) Contour of the second term in (3) which describes the misfit
896 between the predicted vertical rate at the CNSB and that measured by InSAR. c) Contour
897 of the third term in (3) which is sensitive to the presence of undesirable time-invariant
898 contractions in the areas surround the CNSB. d) The total constraint from all three data
899 types, combined using the method discussed in the text. Each panel has a star showing
900 the preferred model ($\eta_{LC}=10^{20.5}$, $\eta_{UM}=10^{19}$ Pa·s).

901

902 Figure 7. Postseismic relaxation velocities predicted from the preferred relaxation model
903 ($\eta_{LC}=10^{20.5}$, $\eta_{UM}=10^{19}$ Pa·s) including the contributions from all the earthquakes

904 considered in this study. a) Red vectors show predicted horizontal velocity to the model
905 faults (majenta line segments) at each GPS site in the compilation of Kreemer et al.,
906 (2007). b) Vertical motion is shown blue for uplift, red for subsidence. Size of the circle
907 indicates the vertical rate.
908
909 Figure 8. a) Dilatational strain rates predicted from the preferred relaxation model
910 velocities ($\eta_{LC}=10^{20.5}$, $\eta_{UM}=10^{19}$ Pa·s). This map was created using the same GPS site
911 locations as the model of Kreemer et al., (2007) (this issue), so that the effects of station
912 distribution on the strain modeling are included. Black arrows indicated the relaxation
913 velocities interpolated onto a regular grid. Quaternary faults are shown with black line
914 traces. State borders and major lakes are shown with faint lines. b) A detailed view of
915 the Northern Walker Lane. The colors now represent the amount of total strain rate,
916 which contains both horizontal shear and dilatation. Black arrow pairs indicate tensor
917 contraction, white arrows tensor extension.
918
919 Figure 9. a) Continuum strain rate model based on the GPS velocity data. This is a detail
920 of the map presented in Kreemer et al., (2007) (this issue). Other features are the same as
921 Figure 9b. b) Same model except based on the time-invariant GPS velocity field
922 obtained by subtracting the preferred relaxation model velocities ($\eta_{LC}=10^{20.5}$, $\eta_{UM}=10^{19}$
923 Pa·s) from the GPS velocities. The zone of deformation has become significantly more
924 focused to the western edge of the Walker Lane.
925

925 **Table 1. Parameters Used for the CNSB Earthquakes**

		Fault Plane					Slip Offset			
Earthquake	**Date**	**Length (km)**	**Width (km)**	**Dip (deg)**		**Strike (deg)**	**Displ. (m)**	**Rake (deg)**	**Mo (N·m)**	**M_W**
Owens Valley	Mar. 26, 1872	100	15	90		339	6	180	2.7E+20	7.6
Pleasant Valley	Oct. 3, 1915	59	21.2	45	W	210	4.0	-90	1.5E+20	7.4
Cedar Mountain	Dec. 21, 1932	60	15.2	80	E	344	2.0	180	5.5E+19	7.1
Combination of		70	19.6	50	E	15	1.0	-159	4.1E+19	7.0
Rainbow Mtn.	Jul. 6, 1954									
Fourmile Flat	Jul. 6, 1954									
Stillwater	Aug. 23, 1954									
Fairview Peak	Dec. 16, 1954	32	17.3	60	E	15	2.4	-126	4.0E+19	7.0
Combination of		22	17.3	60	W	170	0.6	-146	6.9E+18	6.5
Gold King	Dec. 16, 1954									
Louderback	Dec. 16, 1954									
West Gate	Dec. 16, 1954									
Dixie Valley	Dec. 16, 1954	42	23.3	40	E	17	0.9	-90	2.6E+19	6.9

926
927

927 **Table 2. Published Results of Lower Crust/Uppermost Mantle Viscosities for the Basin and**
928 **Range**

Study	Locality	η_{LC} (Pa·s)	η_{UM} (Pa·s)
Geodetic Studies of Modern Earthquakes*			
Pollitz, 2003	ECSZ (Mojave)	3.2×10^{19}	4.6×10^{18}
Pollitz et al., 2001	ECSZ (Hector Mine)	$\eta_{LC} >> \eta_{UM}$	$3\text{-}8 \times 10^{17}$**
Pollitz et al., 2000	ECSZ (Landers)	$\eta_{LC} >> \eta_{UM}$	$1\text{-}6 \times 10^{18}$
Geodetic Studies of Past Earthquakes			
This study	CNSB/WL/EBR	$1\text{-}3 \times 10^{20}$	$1\text{-}3 \times 10^{19}$
Gourmelen and Amelung, 2005	CNSB	$>10^{20}$	$1\text{-}7 \times 10^{18}$
Chang and Smith, 2005	NBR (Hebgen Lk.)	$0.03\text{-}1.3 \times 10^{22}$	$1.3 - 3.2 \times 10^{19}$
Nishimura and Thatcher, 2003	NBR (Hebgen Lk.)	$>10^{20}$	$10^{18}\text{-}10^{20}$
Hetland and Hager, 2003	CNSB	$5\text{-}50 \times 10^{18}$	$>10^{19}$
Dixon et al., 2003	SWL	1×10^{19}	
Geodetic Studies of Large Lake Loading/Unloading			
Bills et al., 2004	WL/CNSB	$2\text{-}10 \times 10^{20}$	$0.6\text{–}10 \times 10^{18}$
Kaufmann and Amelung, 2000	EBR (Lake Mead)	$>10^{20}$	$6\text{-}16 \times 10^{18}$
Adams, et al. 1999	WL/CNSB	--	10^{18}
Bills et al., 1994	EBR (Lk. Bonneville)	$1\text{-}10 \times 10^{20}$	$\sim 10^{19}$
Nakiboglu and Lambeck, 1983	EBR (Lk. Bonneville)	assumed elastic	$2.1 - 34 \times 10^{18}$
Studies of Plate Boundary Dynamics			
Flesch et al., 2000	WL/CNSB	$1\text{-}5 \times 10^{21}$ (whole lithosphere)	

929
930 "—" Indicates no estimate was provided.
931 * "Modern" earthquakes had coseismic deformation observed with space geodesy.
932 ** Tends to increase toward $1\text{-}3 \times 10^{19}$ after 1-3 years of relaxation, indicating transient rheology.
933 CNSB – Central Nevada Seismic Belt, WL – Walker Lane, SWL – Southern Walker Lane, ECSZ
934 – Eastern California Shear Zone, EBR – Eastern Basin and Range, NBR – Northern Basin and
935 Range
936

Table 3. Dilatational Strain Rate ε_Δ for Geodetic Velocities Corrected for Postseismic Relaxation

Domain	Strain Rates				Normalized			
	Observed	Corrected			Observed	Corrected		
		Min.	Max.	Best		Min	Max	Best
Eastern Basin and Range	1.3±1.3	0.8	1.8	1.3	1.0	0.6	1.4	1.0
CNSB	10.5±2.8	-5.7	11.0	3.1	3.8	-2.0	3.9	1.1
Northern Walker Lane	7.2±3.9	6.5	10.3	8.8	1.8	1.7	2.6	2.3
South Walker Lane	3.9±2.9	3.5	7.1	6.3	1.3	1.2	2.4	2.2
Oregon	-3.1±3.4	-3.7	-1.7	-2.5	-0.9	-1.1	-0.5	-0.7
Yucca Mountain	8.0±11.3	5.3	13.3	13.3	0.6	0.5	1.2	1.2

The uncorrected, minimum, maximum and preferred dilatational strain rates ε_Δ and their 1-sigma formal uncertainties are given in units of nanostrains (10^{-9}) per year. Normalized strain rates are the strain rates divided by their formal uncertainties. Values that are greater than 2 or less than –2 indicate 95% significant area growth rate or contractions, respectively. The difference between the maximum and minimum is a measure of the sensitivity of ε_Δ to the viscosity of the lower crust and upper mantle. The "Best" column shows the estimated secular dilatation (corrected for postseismic relaxation) inside each domain given the model with $\eta_{LC}=10^{20.5}$ Pa·s and $\eta_{UM}=10^{19}$ Pa·s.

947

Table 4. Geologic, Geodetic and Relaxation Model Strain Rates Inside Regions.

	Geodetic				Postseismic		Geologic		
Region	ε_Δ	$\pm\sigma\varepsilon$	ε_{xy}	$\pm\sigma\varepsilon$	ε_Δ	ε_{xy}	ε_Δ	ε_{xy}	***R***
East Basin and Range	1.4	1.3	8.9	1.3	0.1	0.2	0.9	1.2	2.9
Walker Lane North	7.3	3.9	33.5	3.9	-0.7	1.1	2.3	7.3	4.9
Walker Lane South	3.9	2.9	79.0	2.9	-1.5	9.2	0.1	15.9	3.9
Oregon	-3.0	3.4	1.0	3.4	-0.1	0.8	1.3	0.9	3.9
Yucca Mountain	8.1	11.3	37.2	11.3	-4.1	1.8	-1.4	10.8	2.0
CNSB (within 180 km)	10.5	2.8	23.5	2.8	10.3	14.7	2.3	2.7	5.1
CNSB (within 70km)	31.0	10.3	48.4	10.3	23.9	34.0	1.7	2.3	9.5

Velocities used to calculate geodetic strain rates and uncertainties have not been corrected for postseismic relaxation, and are from the strain rate model of Kreemer et al., 2007 (this volume). Geologic strain rates are from the UQFD, obtained in equation (1) and shown in Figure 2. Postseismic strain rates come from the viscoelastic relaxation model. Strain rates are in nanostrains/yr.

948
949

REFERENCES CITED

Adams, K.D., S.G. Wesnousky, and B.G. Bills, 1999, Isostatic rebound, active faulting, and potential geomorphic effects in the Lake Lahontan Basin, Nevada and California: GSA Bulletin, v. 111, p. 1739-1756.

Allmendinger, R.W., T.A. Hauge, E.C. Hauser, C.J. Potter, S.L. Klemperer, K.D. Nelson, P. Knuepfer, and J. Oliver, 1987, Overview of the COCORP 40˚N transect, western United States: The fabric of an orogenic belt: Geological Society of America Bulletin, v. 98, p. 308-319.

Beanland, S., and M.M. Clark, 1994, The Owens Valley fault zone, eastern California, and surface rupture associated with the 1872 earthquake: U.S. Geological Survey Bulletin, v. 1982, p. 1-29.

Bell, J.W., S.J. Caskey, A.R. Ramelli, and L. Guerrieri, 2004, Pattern and rates of faulting in the central Nevada seismic belt, and paleoseismic evidence for prior belt-like behavior: Bulletin of the Seismological Society of America, v. 94, p. 1229-1254.

Bell, J.W., C.M. dePolo, A.R. Ramelli, A.M. Sarna-Wojcicki, and C.E. Meyer, 1999, Surface faulting and paleoseismic history of the 1932 Cedar Mountain earthquake area, west-central Nevada, and implications for modern tectonics of the Walker Lane: GSA Bulletin, v. 111, p. 791-807.

Bennett, R.A., B.P. Wernicke, and J.L. Davis, 1998, Continuous GPS measurements of contemporary deformation across the northern Basin and Range province: Geophysical Research Letters, v. 25, p. 563-566.

Bennett, R.A., B.P. Wernicke, N.A. Niemi, A.M. Friedrich, and J.L. Davis, 2003, Contemporary strain rates in the northern Basin and Range province from GPS data: Tectonics, v. 22, 1008, doi:10.1029/2001TC001355.

Benz, H.M., R.B. Smith, and W.D. Mooney, 1990, Crustal structure of the northwestern Basin and Range province from the 1986 Program for Array Seismic Studies of the Continental Lithosphere seismic experiment: Journal of Geophysical Research, v. 95, p. 21,823 - 21,842.

Bills, B.G., K.D. Adams, and S.G. Wesnousky, 2004, Viscosity structure of the crust and upper mantle in western Nevada from isostatic rebound patterns of Lake Lahontan shorelines: Geophysical Journal International, v. in press.

Bills, B.G., D.R. Currey, and G.A. Marshall, 1994, Viscosity estimates for the crust and upper-mantle from patterns of shoreline deformation in the Eastern Great Basin: Journal of Geophysical Research, v. 99, p. 22,059-22,086.

Bills, B.G., and G.M. May, 1987, Lake Bonneville: Constraints on lithospheric thickness and upper mantle viscosity from isostatic warping of Bonneville, Provo and Gilbert stage shorelines: Journal of Geophysical Research, v. 92, p. 11,493-11,508.

Blackwell, D.D., and J.L. Steele, 1992, Geothermal map of North America: Boulder, CO, Geological Society of America.

Blewitt, G., D.F. Argus, R.A. Bennett, Y. Bock, E. Calais, M. Craymer, J.L. Davis, T.H. Dixon, J.T. Freymueller, T.A. Herring, D. Johnson, K.M. Larson, E.L. Miller, G.F. Sella, R.A. Snay, and M. Tamissiea, 2005, A stable North America reference

frame (SNARF): First release, UNAVCO-IRIS Joint Workshop: Stevenson, Washington.
Block, L., and L.H. Royden, 1990, Core complex geometries and regional scale flow in the lower crust: Tectonics, v. 9, p. 557-567.
Cao, T., W.A. Bryant, B. Rowshandel, D. Branum, and C.J. Wills, 2003, The revised 2002 California probabilistic seismic hazard maps, Open-File Report 96-08, California Geological Survey.
Caskey, J.S., J.W. Bell, A.R. Ramelli, and S.G. Wesnousky, 2004, Historic surface faulting and paleoseismicity in the area of the 1954 Rainbow Mountain-Stillwater earthquake sequence, central Nevada: Bulletin of the Seismological Society of America, v. 94, p. 1255-1275.
Caskey, J.S., J.W. Bell, B.D. Slemmons, and A.R. Ramelli, 2000, Historical surface faulting and paleoseismology of the central Nevada seismic belt, *in* Lageson, D.R., Peters, S.G., and Lahren, M.M., eds., Geological Society of America Field Guide 2: Boulder, Colorado, p. 23-44.
Caskey, J.S., S.G. Wesnousky, P. Zhang, and B.D. Slemmons, 1996, Surface faulting of the 1954 Fairview Peak (Ms=7.2) and Dixie Valley (Ms=6.9) earthquakes, central Nevada: Bulletin of the Seismological Society of America, v. 86, p. 761-787.
Chang, W.-L., and R.B. Smith, 2005, Lithospheric rheology from post-seismic deformation of a M7.5 normal faulting earthquake with implications for continental kinematics: Journal of Geophysical Research, v. submitted.
DeMets, C., and T.H. Dixon, 1999, New kinematic models for Pacific-North America motion from 3 Ma to present: I. Evidence for steady motion and biases in the NUVEL-1A model: Geophysical Research Letters, v. 26, p. 1921-1924.
dePolo, C.M., and J.G. Anderson, 2000, Estimating the slip rates of normal faults in the Great Basin, USA: Basin Research, v. 12, p. 227-240.
Dixon, T.H., E. Norabuena, and H. L., 2003, Paleoseismology and Global Positioning System: Earthquake-cycle effects and geodetic versus geologic fault slip rates in the eastern California shear zone: Geology, v. 31, p. 55-58.
Doser, D.I., 1986, Earthquake processes in the Rainbow Mountain-Fairview Peak-Dixie Valley, Nevada, Region 1954-1959: Journal of Geophysical Research, v. 91, p. 12,572-12,586.
—, 1988, Source parameters of earthquakes in the Nevada seismic zone, 1915-1943: Journal of Geophysical Research, v. 93, p. 15,001-15,015.
Dziewonski, A.M., and D.L. Anderson, 1981, Preliminary reference Earth model: Physics of the Earth and Planetary Interiors, v. 25, p. 297-356.
Faulds, J.E., C.D. Henry, N.H. Hinz, P.S. Drakos, and B. Delwiche, 2005, Transect across the northern Walker Lane, northwest Nevada and northeast California: An incipient transform fault along the Pacific-North American plate boundary, *in* Pederson, J., and Dehler, C.M., eds., Interior Western United States: Geological Society of America Field Guide 6.
Fialko, Y., 2004, Evidence of fluid-filled upper crust from observations of postseismic deformation due to the 1992 M27.3 Landers earthquake: Journal of Geophysical Research, v. 109.

1038 Flesch, L.M., W.E. Holt, A.J. Haines, and B. Shen-Tu, 2000, Dynamics of the Pacific-
1039 North America plate boundary in the western United States: Science, v. 287, p.
1040 834-836.
1041 Freed, A.M., and R. Burgmann, 2004, Evidence of power-law flow in the Mojave Desert
1042 mantle: Nature, v. 430, p. 548-551.
1043 Freund, L.B., and D.M. Barnett, 1976, A two-dimensional analysis of surface
1044 deformation due to dip-slip faulting: Bulletin of the Seismological Society of
1045 America, v. 66, p. 667-675.
1046 Friedrich, A.M., J. Lee, B.P. Wernicke, and K. Sieh, 2004, Geologic context of geodetic
1047 data across a Basin and Range normal fault, Crescent Valley, Nevada: Tectonics,
1048 v. 23, p. -.
1049 Friedrich, A.M., B.P. Wernicke, N.A. Niemi, R.A. Bennett, and G.A. Davis, 2003,
1050 Comparison of geodetic and geologic data from the Wasatch region, Utah, and
1051 implications for the spectral character of Earth deformation at periods of 10 to 10
1052 million years: Journal of Geophysical Research, v. 108, p. 2199.
1053 Gans, P.B., 1987, An open-system, two-layer crustal stretching model for the eastern
1054 great basin: Tectonics, v. 6, p. 1-12.
1055 Gilbert, H., and A.F. Sheehan, 2004, Images of crustal variations in the intermountain
1056 west: Journal of Geophysical Research, v. 109.
1057 Gourmelen, N., and F. Amelung, 2005, Post-seismic deformation in the central Nevada
1058 seismic belt detected by InSAR: Implications for Basin and Range dynamics:
1059 Science, v. 310, p. 1473-1476.
1060 Haller, K.M., R.L. Wheeler, and K.S. Rukstales, 2002, Documentation of changes in fault
1061 parameters for the 2002 National Seismic Hazard Maps - Conterminous United
1062 States except California, Open-File Report 02-467, U.S. Geological Survey, p. 34.
1063 Hammond, W.C., and W. Thatcher, 2004, Contemporary tectonic deformation of the
1064 Basin and Range province, western United States: 10 years of observation with
1065 the Global Positioning System: Journal of Geophysical Research, v. 109, B08403,
1066 doi:10.1029/2003JB002746.
1067 —, 2005, Northwest Basin and Range tectonic deformation observed with the Global
1068 Positioning System, 1999-2003: Journal of Geophysical Research, v. 110,
1069 B10405, doi:10.1029/2005JB003678.
1070 Hammond, W.C., W. Thatcher, and G. Blewitt, 2004, Crustal deformation across the
1071 Sierra Nevada-northern Walker Lane, Basin and Range transition, western United
1072 States measured with GPS, 2000-2004: Eos Transactions AGU Fall Meeting
1073 Supplement, v. 85.
1074 Hearn, E.H., 2003, What can GPS data tell us about the dynamics of post-seismic
1075 deformation?: Geophysical Journal International, v. 155, p. 753-777.
1076 Hetland, E.A., and B.H. Hager, 2003, Postseismic relaxation across the Central Nevada
1077 Seismic Belt: Journal of Geophysical Research, v. 108, 2394,
1078 doi:10.1029/2002JB002257.
1079 Hodgkinson, K.M., R.S. Stein, and G. Marshall, 1996, Geometry of the 1954 Fairview
1080 Peak-Dixie Valley earthquake sequence from a joint inversion of leveling and
1081 triangulation data: Journal of Geophysical Research, v. 101, p. 25,437-25,457.

1082 Holbrook, S.W., 1990, The crustal structure of the northwestern Basin and Range
1083 province, Nevada, from wide-angle seismic data: Journal of Geophysical
1084 Research, v. 95, p. 21,843-21,869.
1085 Jackson, J., 2002, Strength of the continental lithosphere; time to abandon the jelly
1086 sandwich?: GSA Today, v. 12, p. 4-10.
1087 Kaufmann, G., and F. Amelung, 2000, Reservoir-induced deformation and continental
1088 rheology in vicinity of Lake Mead, Nevada: Journal of Geophysical Research, v.
1089 105, p. 16,341-16,358.
1090 Kostrov, V.V., 1974, Seismic moment and energy of earthquakes, and seismic flow of
1091 rocks: Izv. Acad. Sci. USSR Phys. Solid Earth, v. 1 (English Translation), p. 23-
1092 44.
1093 Kreemer, C., G. Blewitt, and W.C. Hammond, 2007, Geodetic constraints on
1094 contemporary deformation in the northern Walker Lane: 2, velocity and tensor
1095 strain rate analysis: Late Cenozoic Structure and Evolution of the Great Basin –
1096 Sierra Nevada Transition.
1097 Lachenbruch, A.H., and J.H. Sass, 1978, Models of extending lithosphere and heat flow
1098 in the Basin and Range province, *in* Smith, R.B., and Eaton, G.P., eds., Cenozoic
1099 Tectonics and Regional Geophysics of the Western Cordillera, Memoir 152:
1100 Boulder, Colorado, Geological Society of America, p. 209-250.
1101 Lee, J., J. Spencer, and L. Owen, 2001, Holocene slip rates along the Owens Valley
1102 Fault, California; Implications for the recent evolution of the Eastern California
1103 Shear zone: Geology, v. 29, p. 819-822.
1104 Lowry, A.R., and R.B. Smith, 1995, Strength and rheology of the western U.S. cordillera:
1105 Journal of Geophysical Research, v. 100, p. 17,947-17,963.
1106 McCaffrey, R., M.D. Long, C. Goldfinger, P.C. Zwick, J.L. Nabelek, C.K. Johnson, and
1107 C. Smith, 2000, Rotation and plate locking at the southern Cascadia subduction
1108 zone: Geophysical Research Letters, v. 27, p. 3117-3120.
1109 Miller, M.M., D.J. Johnson, and T.H. Dixon, 2001a, Refined kinematics of the eastern
1110 California shear zone from GPS observations, 1993-1998: Journal of Geophysical
1111 Research, v. 106, p. 2245-2263.
1112 Miller, M.M., D.J. Johnson, C.M. Rubin, H. Dragert, K. Wang, A. Qamar, and C.
1113 Goldfinger, 2001b, GPS-determination of along-strike variation in Cascadia
1114 margin kinematics: Implications for relative plate motion, subduction zone
1115 coupling, and permanent deformation: Tectonics, v. 20, p. 161-176.
1116 Murray, J.R., P. Segall, P. Cervelli, W.H. Prescott, and J.L. Svarc, 2001, Inversion of
1117 GPS data for spatially variable slip-rate on the San Andreas Fault near Parkfield,
1118 CA: Geophysical Research Letters, v. 28, p. 359-362.
1119 Nakiboglu, S.M., and K. Lambeck, 1983, A reevaluation of the isostatic rebound of Lake
1120 Bonneville: Journal of Geophysical Research, v. 88, p. 10439-10447.
1121 Nishimura, T., and W. Thatcher, 2003, Rheology of the lithosphere inferred from
1122 postseismic uplift following the 1959 Hebgen Lake earthquake: Journal of
1123 Geophysical Research, v. 108.
1124 Nur, A., and G. Mavko, 1974, Postseismic viscoelastic rebound: Science, v. 183, p. 204-
1125 206.
1126 Oldow, J.S., 2003, Active transtensional boundary zone between the western Great Basin
1127 and Sierra Nevada block, western U.S. Cordillera: Geology, v. 31, p. 1033-1036.

1128 Oldow, J.S., C.L.V. Aiken, J.L. Hare, J.F. Ferguson, and R.F. Hardyman, 2001, Active
1129 displacement transfer and differential block motion within the central Walker
1130 Lane, western Great Basin: Geology, v. 29, p. 19-22.
1131 Pancha, A., J.G. Anderson, and C. Kreemer, 2006, Comparison of seismic and geodetic
1132 scalar moment rates across the Basin and Range province: Bulletin of the
1133 Seismological Society of America, v. 96, p. 11-32, doi:10.1785/0120040166.
1134 Pollitz, F.F., 1997, Gravitational-viscoelastic postseismic relaxation on a layered
1135 spherical Earth: Journal of Geophysical Research, v. 102, p. 17,921-17,941.
1136 —, 2003, Transient rheology of the uppermost mantle beneath the Mojave Desert,
1137 California: Earth and Planetary Science Letters, v. 215, p. 89-104.
1138 Pollitz, F.F., W.H. Bukun, and M. Nyst, 2004, A physical model for strain accumulation
1139 in the San Francisco Bay region: Stress evolution since 1838: Journal of
1140 Geophysical Research, v. 109.
1141 Pollitz, F.F., G. Peltzer, and R. Burgmann, 2000, Mobility of continental mantle:
1142 Evidence from postseismic geodetic observation following the 1992 Landers
1143 earthquake: Journal of Geophysical Research, v. 105, p. 8035-8054.
1144 Pollitz, F.F., C.W. Wicks, and W. Thatcher, 2001, Mantle Flow Beneath a Continental
1145 Strike Slip Fault: Postseismic Deformation After the 1999 Hector Mine
1146 Earthquake: Science, v. 293, p. 1814-1818.
1147 Savage, J.C., and R.O. Burford, 1973, Geodetic determination of relative plate motion in
1148 central California: Journal of Geophysical Research, v. 78, p. 832-845.
1149 Savage, J.C., W. Gan, and J.L. Svarc, 2001, Strain accumulation and rotation in the
1150 eastern California shear zone: Journal of Geophysical Research, v. 106, p. 21,995-
1151 22,007.
1152 Savage, J.C., and L.M. Hastie, 1969, A dislocation model for the Fairview Peak, Nevada,
1153 earthquake: Bulletin of the Seismological Society of America, v. 59, p. 1937-
1154 1948.
1155 Savage, J.C., M. Lisowski, J.L. Svarc, and W.K. Gross, 1995, Strain accumulation across
1156 the central Nevada seismic zone, 1973-1994: Journal of Geophysical Research, v.
1157 100, p. 20,257-20,269.
1158 Savage, J.C., and W.H. Prescott, 1978, Asthenosphere readjustment and the earthquake
1159 cycle: Journal of Geophysical Research, v. 83, p. 3369-3376.
1160 Sawyer, T.L., R.W. Briggs, and A.R. Ramelli, 2005, Late Quaternary Activity of the
1161 Southern Mohawk Valley fault zone, northeastern California: Seismological
1162 Research Letters, v. 76, p. 248.
1163 Sella, G.F., T.H. Dixon, and A. Mao, 2002, REVEL: A model for recent plate velocities
1164 from space geodesy: Journal of Geophysical Research, v. 107, p.
1165 10.1029/2000JB000033.
1166 Shen-Tu, B., W.E. Holt, and J.A. Haines, 1999, Deformation kinematics in the western
1167 United States determined from Quaternary fault slip rates and recent geodetic
1168 data: Journal of Geophysical Research, v. 104, p. 28,927-28,955.
1169 Slemmons, B.D., 1957, Geological effects of the Dixie Valley-Fairview Peak, Nevada
1170 earthquakes of December 16, 1954: Bulletin of the Seismological Society of
1171 America, v. 47, p. 353-375.
1172 Snay, R.A., M.W. Cline, and E.L. Timmermann, 1985, Dislocation models for the 1954
1173 earthquake sequence in Nevada: USGS Open File Report 89-290, p. 531-555.

Svarc, J.L., J.C. Savage, W.H. Prescott, and M.H. Murray, 2002a, Strain accumulation and rotation in western Oregon and southwestern Washington: Journal of Geophysical Research, v. 107, doi:10.1029/2001JB000625.

Svarc, J.L., J.C. Savage, W.H. Prescott, and A.R. Ramelli, 2002b, Strain accumulation and rotation in western Nevada, 1993-2000: Journal of Geophysical Research, v. 107, p. 10.1029/2001JB000579.

Thatcher, W., G.R. Foulger, B.R. Julian, J.L. Svarc, E. Quilty, and G.W. Bawden, 1999, Present-day deformation across the Basin and Range province, western United States: Science, v. 283, p. 1714-1718.

Wallace, R.E., 1984a, Faulting related to the 1915 earthquakes in Pleasant Valley, Nevada: U.S. Geological Survey Professional Paper, v. 1274-A,B, p. A1-A33.

—, 1984b, Patterns and timing of late quaternary faulting in the Great Basin province and relation to some regional tectonic features: Journal of Geophysical Research, v. 89, p. 5763-5769.

Wernicke, B.P., A.M. Friedrich, N.A. Niemi, R.A. Bennett, and J.L. Davis, 2000, Dynamics of plate boundary fault systems from Basin and Range Geodetic Network (BARGEN) and Geologic Data: GSA Today, v. 10, p. 1-7.

Wesnousky, S.G., A.D. Baron, R.W. Briggs, J.S. Caskey, S.J. Kumar, and L. Owen, 2005, Paleoseismic transect across the northern Great Basin: Journal of Geophysical Research, v. 110, B05408, doi:10.1029/2004JB003283.

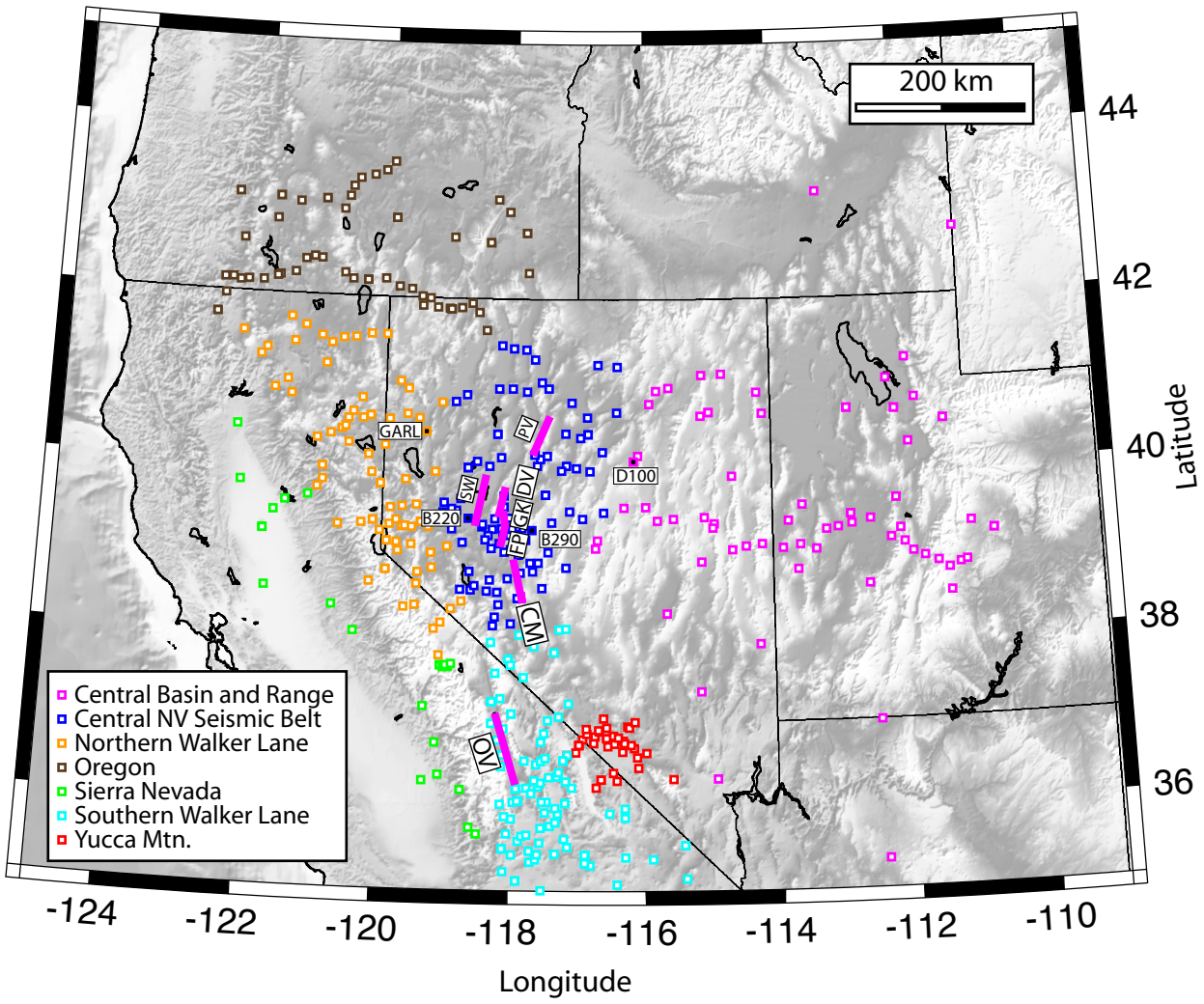

Figure 1. Hammond, Kreemer, Blewitt 2006

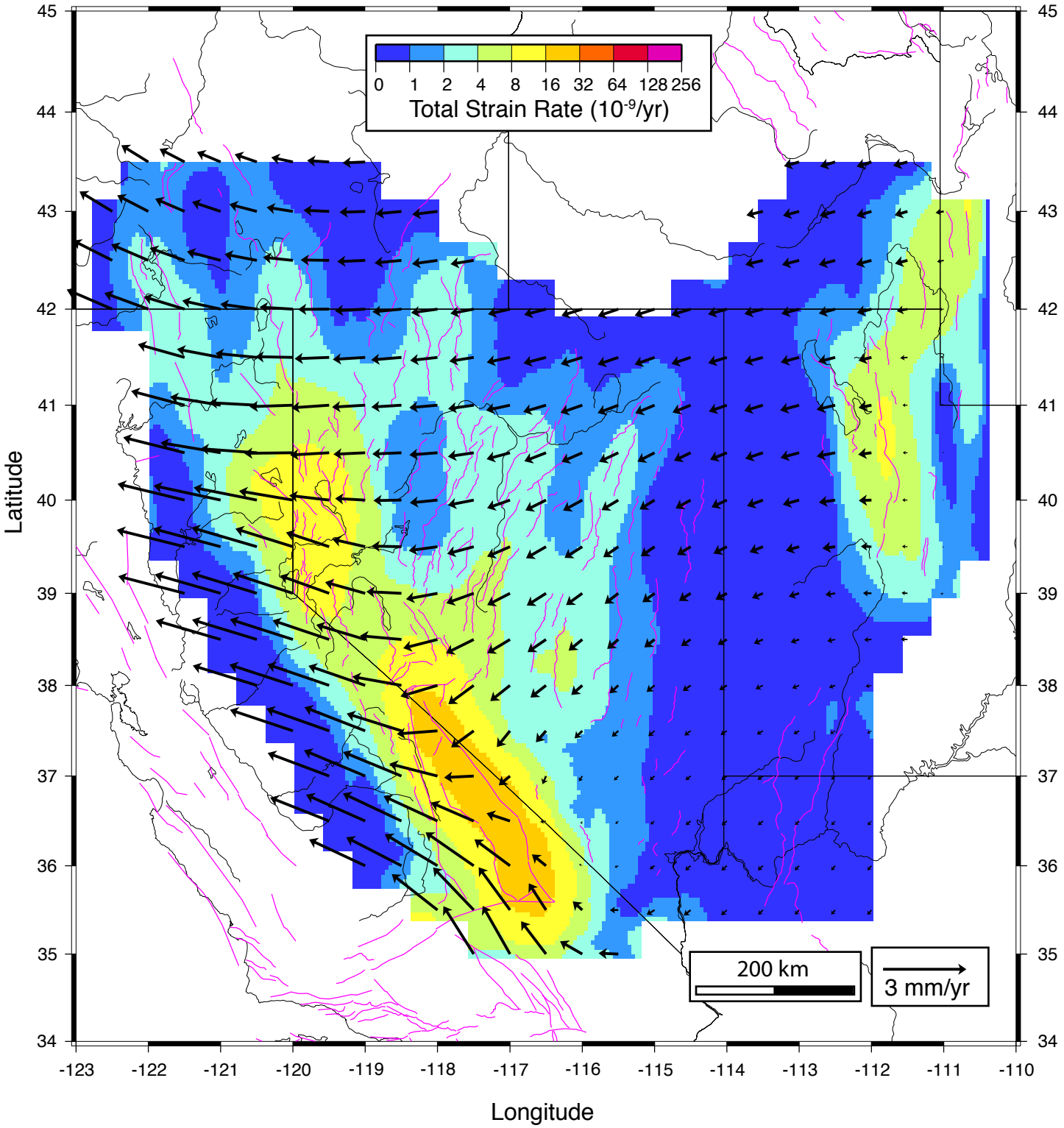

Figure 2. Hammond, Kreemer, Blewitt 2006

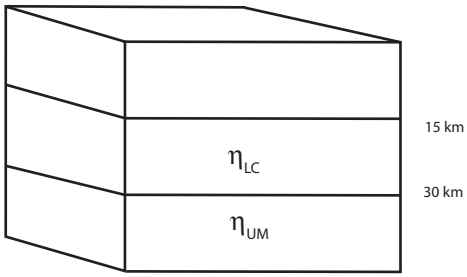

Figure 3. Hammond, Kreemer, Blewitt 2006

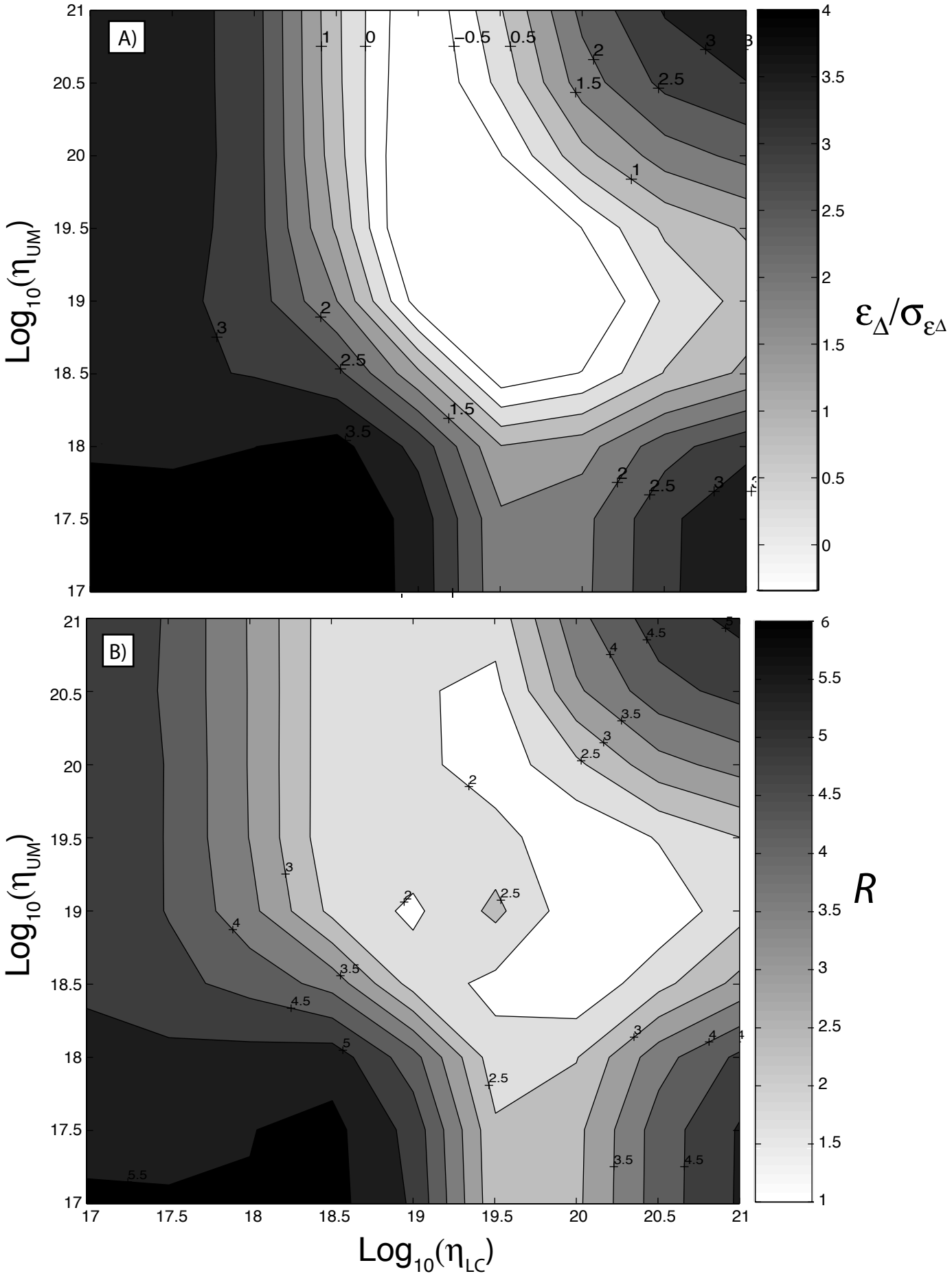

Figure 4. Hammond, Kreemer, Blewitt 2006

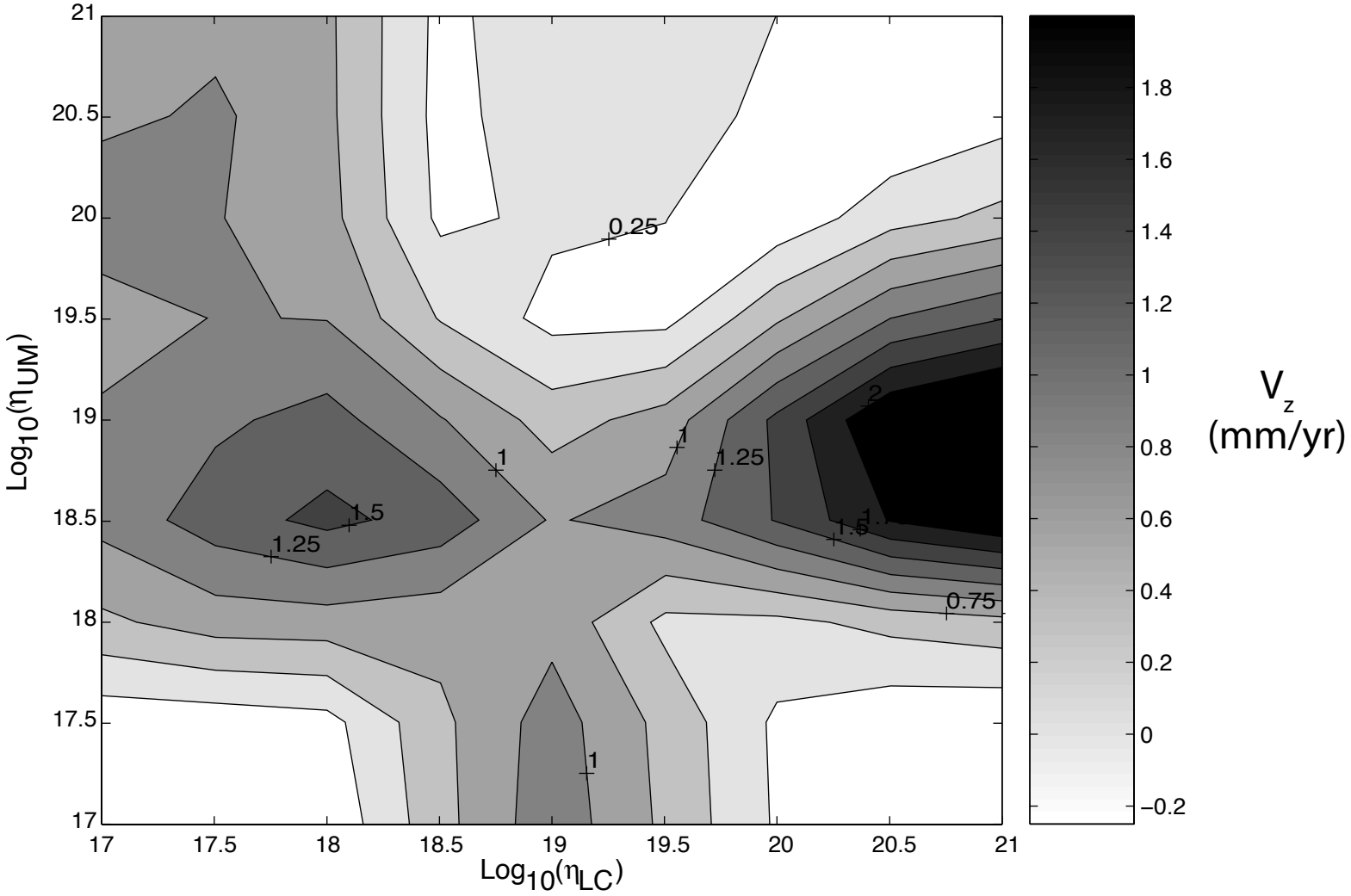

Figure 5. Hammond, Kreemer, Blewitt 2006

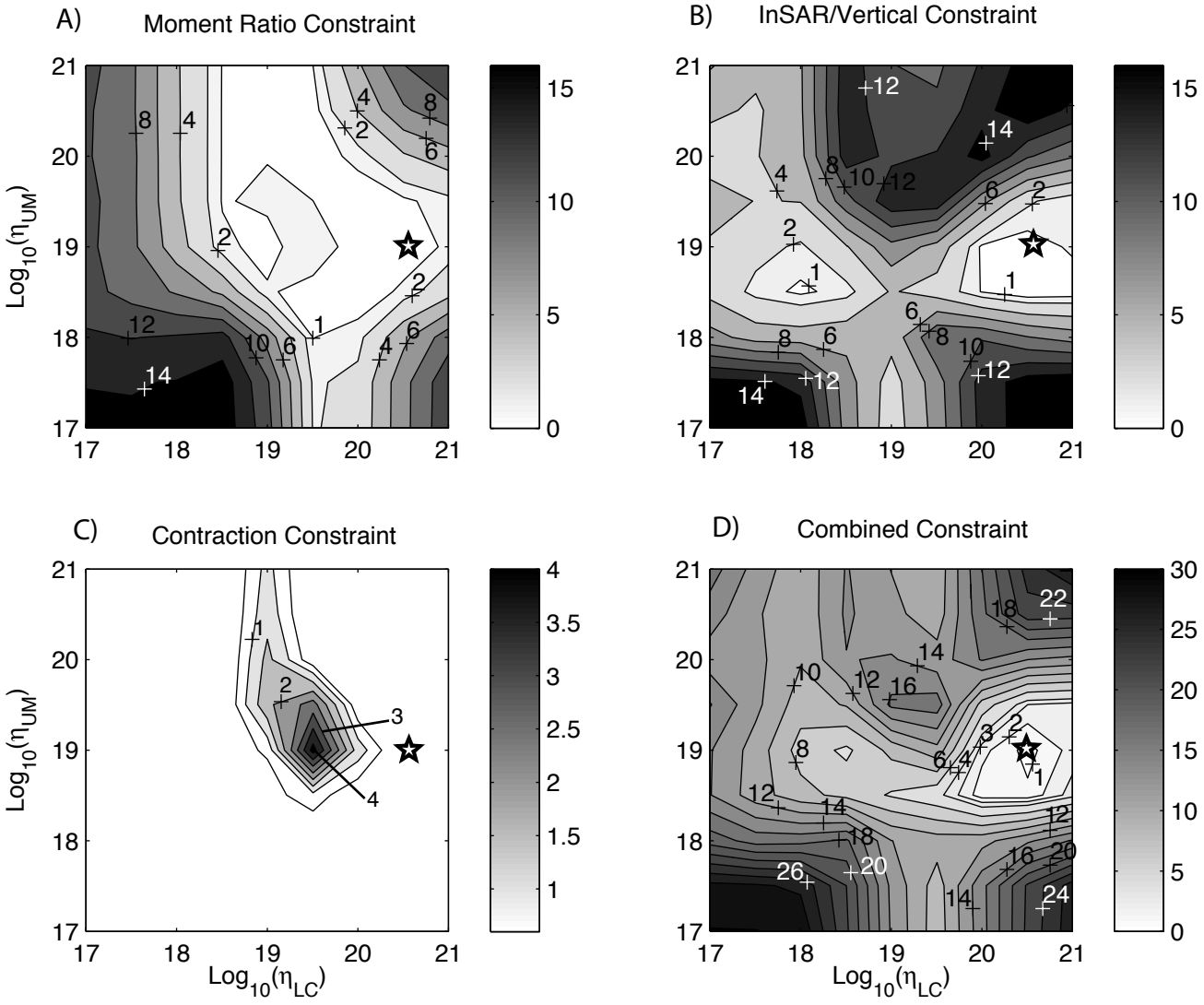

Figure 6. Hammond, Kreemer, Blewitt 2006

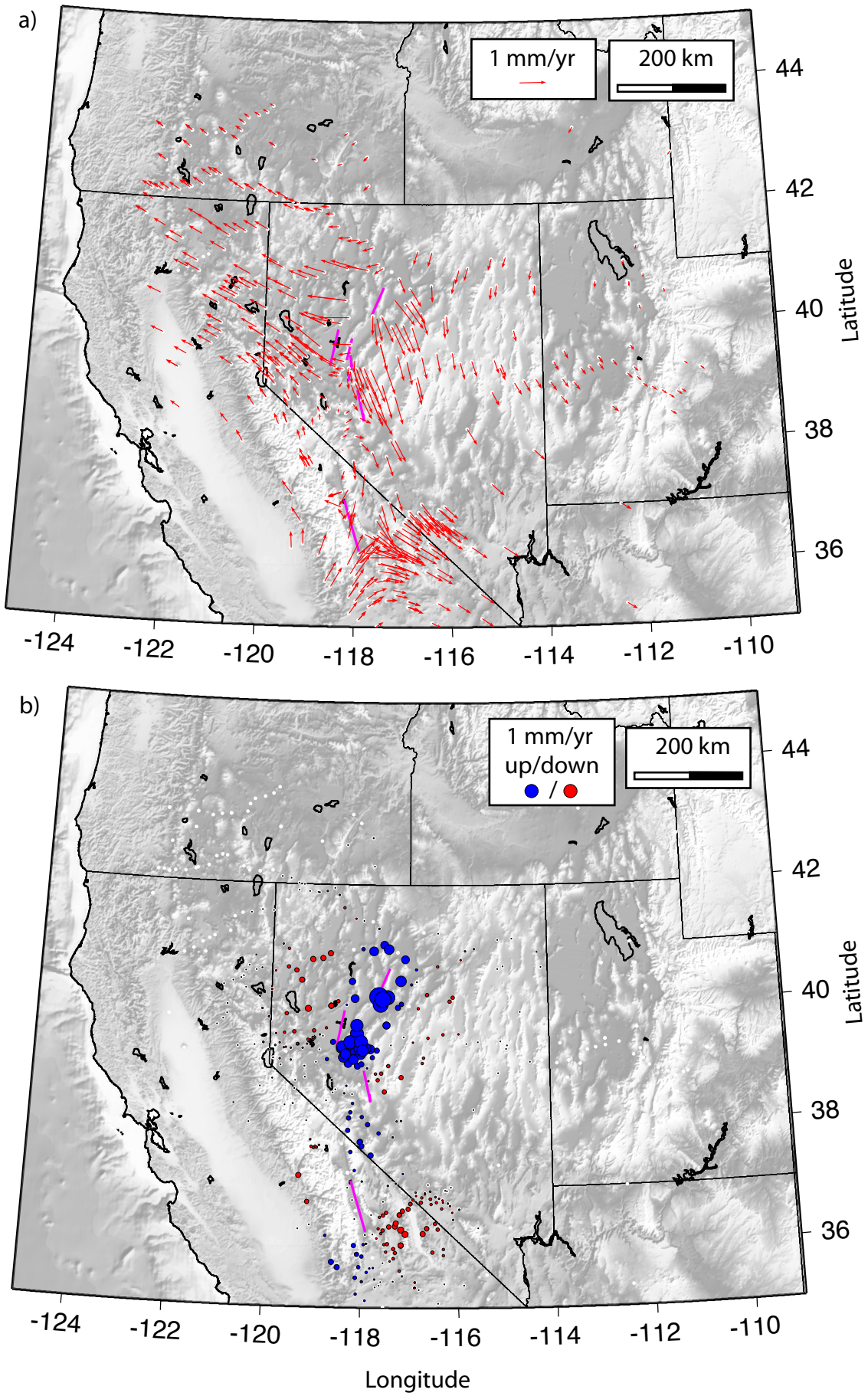

Figure 7. Hammond, Kreemer, Blewitt 2006

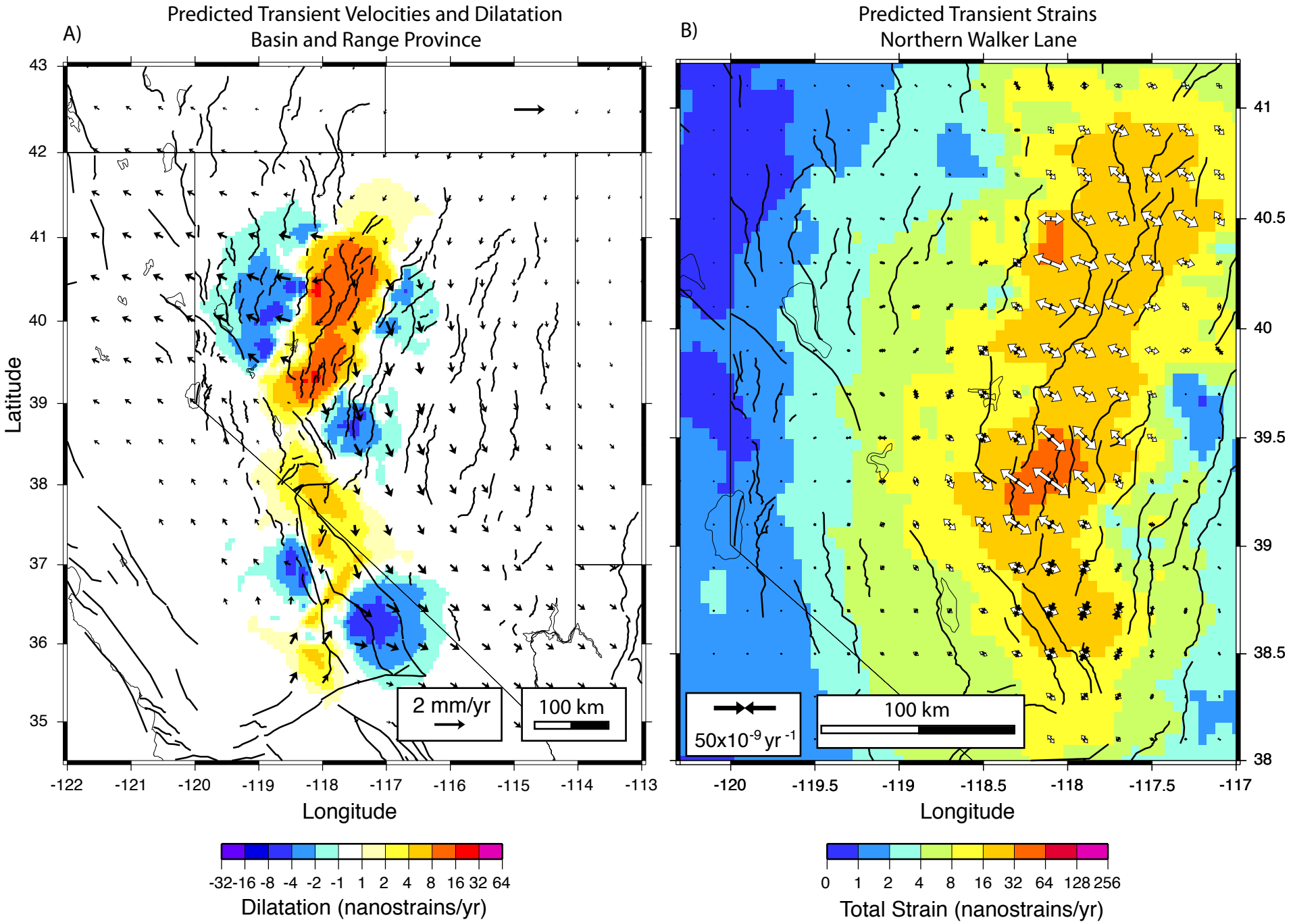

Figure 8. Hammond, Kreemer, Blewitt 2006

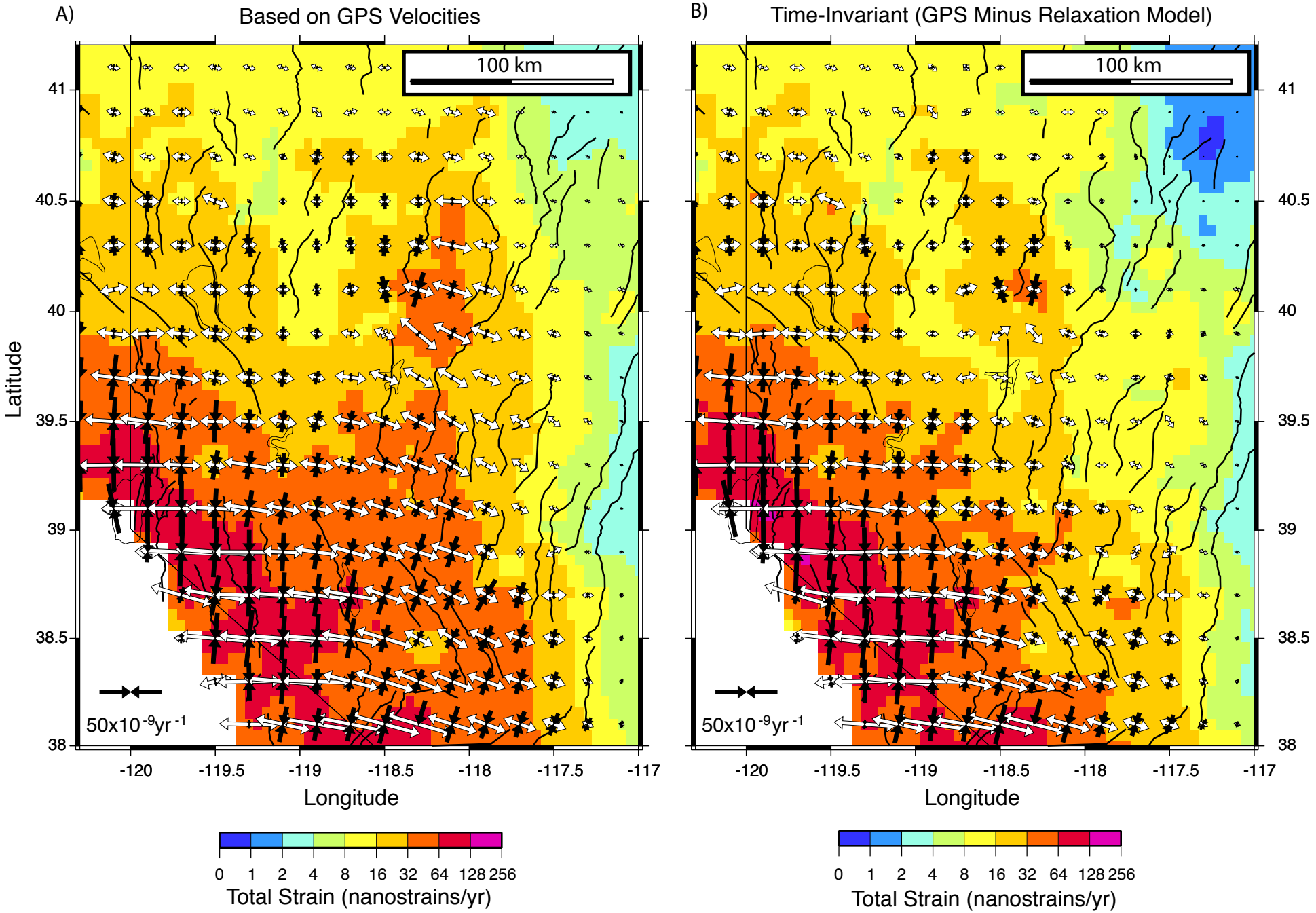

Figure 9. Hammond, Kreemer, Blewitt 2006